https://doi.org/10.5194/egusphere-2023-375
Preprint. Discussion started: 5 April 2023

Development of Inter-Grid Cell Lateral Unsaturated and Saturated Flow Model in the E3SM Land Model (v2.0)

Han Qiu[1], Gautam Bisht[1], Lingcheng Li[1], Dalei Hao[1], and Donghui Xu[1]

[1]Atmospheric Sciences and Global Change Division, Pacific Northwest National Laboratory, Richland, WA, USA

Correspondence: Han Qiu (han.qiu@pnnl.gov)

Abstract. The lateral transport of water in the subsurface is important in modulating the terrestrial water-energy distribution. Although few land surface models have recently included lateral saturated flow within and across grid cells, it is not a default configuration in the Climate Model Intercomparison Project version 6 experiments. In this work, we developed the lateral subsurface flow model with both unsaturated and saturated zones in the Energy Exascale Earth System Model (E3SM) Land Model version 2 (ELMv2.0). The new model, called ELM$_{lat}$, was benchmarked against PFLOTRAN, a 3D subsurface flow and transport model, for three idealized hillslopes that included a convergent hillslope, divergent hillslope, and titled V-shape hillslope with variably saturated initial conditions. ELM$_{lat}$ showed comparable performance with PFLOTRAN in terms of capturing the dynamics of soil moisture and groundwater table for the three benchmark hillslope problems. Specifically, the mean absolute errors (MAE) of the soil moisture in the top five layers between ELM$_{lat}$ and PFLOTRAN were within $1\% \pm 4\%$ and the MAE of water table depth were within ± 0.3 m. Next ELM$_{lat}$ was applied to the Little Washita experimental watershed to assess its prediction of groundwater table, soil moisture, and soil temperature. The spatial pattern of simulated groundwater table depth agreed well with the global groundwater table benchmark dataset generated from a global model calibrated with long term observations. The effects of lateral groundwater flow on the energy flux partitioning were more prominent in low land areas with shallower groundwater tables, which the difference of simulated annual surface soil temperature could reach $0.4 - 0.5\ ^{\circ}C$ at low land areas between ELMv2.0 and ELM$_{lat}$. Incorporating lateral subsurface flow in ELM improves the representation of the subsurface hydrology which will provide a good basis for future large-scale applications.

1 Introduction

Groundwater, which stores $\sim 30\%$ of the world's freshwater, plays an important role in the global hydrologic cycle and is a critical water resource for the environment and human systems. As the bottom boundary, groundwater moderates soil moisture that is extracted by vegetation roots while is recharged by water percolation and acts as an important buffer in the water cycle (Maxwell et al., 2007; Fan et al., 2007; Miguez-Macho et al., 2007; Fan, 2015). Groundwater also interacts with rivers by supporting the base flow or receiving the percolated water from rivers and feeds the groundwater dependent wetlands (De Graaf et al., 2014; de Graaf et al., 2017; Condon and Maxwell, 2019; Qiu et al., 2019). Groundwater is a major freshwater resource for drinking and irrigation, and has been used for various industrial purposes (Döll et al., 2012; Wada et al., 2011). With the surging growth of population and water demand, overexploitation of groundwater resources have been witnessed world

https://doi.org/10.5194/egusphere-2023-375
Preprint. Discussion started: 5 April 2023

wide (Wada et al., 2010, 2012; Gleeson et al., 2012; Pokhrel et al., 2015) , which unsustainably impacted the long term water supplies and impaired the health of many ecosystems (Wada et al., 2012; Gleeson et al., 2012).

Improving the representations of groundwater flow in Land Surface Models (LSMs), which serve as the land component of Earth System Models (ESMs) could promote the address of important scientific questions (Clark et al., 2015). Groundwater movement in the critical zone, usually defined as the shallow groundwater (between 1-5 m), is important in modulating the terrestrial water-energy distribution and land-atmosphere interactions (Kollet and Maxwell, 2008; Condon and Maxwell, 2019; Fan, 2015). Long term groundwater movement and storage variations are found highly influential in predicting the long-term water and energy partitions across different scales (Wang, 2012; Fang et al., 2016; Zhang et al., 2022). All these factors determine the important role that groundwater is playing in regulating the eco-hydrological processes, especially in the groundwater supplied ecosystems (Chui et al., 2011; Miguez-Macho and Fan, 2012; Subin et al., 2014; Vrettas and Fung, 2017; Fang et al., 2022). Moreover, the role of groundwater in regulating the water and energy balances at the land/atmosphere interface and how its feedback to climate change would affect ecosystem functioning at various spacial and temporal scales remain partly understood (Kløve et al., 2014; Clark et al., 2015). Lateral groundwater flow represents a critical process in representing groundwater dynamics. The magnitude of lateral groundwater flow is suggested to be scaling with grid resolution (Krakauer et al., 2014). With grid resolution less than $0.1^o(10\ km)$, lateral flow is comparable to the recharge rate and thus is non-negligible (Krakauer et al., 2014). Therefore, incorporating detailed representations of the lateral groundwater flow is important in LSMs regarding the surging interests in Hyper-resolution modeling at regional or global scales (Wood et al., 2011; Bierkens et al., 2015; Fan et al., 2019).

Despite the importance of groundwater systems in the terrestrial processes, incorporation of lateral groundwater flow models in LSMs is just nascent. Nearly all LSMs that participated in the Climate Model Intercomparison Project version 6 (Eyring et al., 2016) ignored lateral groundwater flow. Most of these LSMs simulate vertical only soil water movement without lateral connections and parameterize the saturated groundwater dynamics with a lumped unconfined aquifer, e.g. CLM4.5 (Oleson et al., 2013), HiGW-MAT (Pokhrel et al., 2015). A few recent works have incorporated lateral groundwater flow within/across grids in LSMs. For example, Swenson et al. (2019) incorporated intra-grid saturated lateral groundwater flow into Community Land Model (CLM) v5.0 at the hillslope scale. Recently, a number of inter-grid cell lateral groundwater flow models have been developed, which can be categorized into two major groups. The first group solves quasi three dimensional (3-D) groundwater flow that accounts for vertical soil water movement in the unsaturated zone and only lateral groundwater flow in the saturated zone. For example, Zeng et al. (2018) coupled a lateral groundwater flow model in the saturated zone with CLMv4.5 (Oleson et al., 2013); Felfelani et al. (2021) extended the work of Swenson et al. (2019) to include inter-grid cell saturated lateral groundwater flow in CLM5.0 and applied the model at continental scale; Chaney et al. (2016, 2021) developed the HydroBlocks model by coupling the dynamic TOPMODEL, which used a kinematic wave approach and recently updated to Darcy flux, to represent the saturated lateral flow, with Noah-MP; H3D model (Troch et al., 2003; Paniconi et al., 2003; Hazenberg et al., 2015) couples a vertical 1-D soil column model with a pseudo-2D saturated groundwater model and was validated with a 3-D Richards equation model (Richards, 1931); similarly, PAWS (Shen and Phanikumar, 2010; Shen et al., 2013) solves the saturation based (θ-based) 1-D Richards equation in the unsaturated zone and 2-D diffusive groundwater

https://doi.org/10.5194/egusphere-2023-375
Preprint. Discussion started: 5 April 2023

equation in the saturated zone, and was coupled with CLMv4.0 for solving land surface processes. The second group solves fully 3-D groundwater flow in both the saturated and unsaturated zones. For example, ParFlow solves the variably saturated 3-D Richards equation for both unsaturated and saturated groundwater and has a comprehensive representation of the surface and subsurface processes (Kollet and Maxwell, 2006, 2008; Maxwell, 2013). CLM-PFLOTRAN couples PFLOTRAN (Hammond and Lichtner, 2010) with CLM4.5 (**?**) , which simulates the 3-D subsurface flow by solving the 3-D variably saturated Richards equation and represents the land surface processes with CLM4.5 (Bisht et al., 2017); Similarly, Miura and Yoshimura (2020) developed the 3-D Variably saturated groundwater model considering the storativity of groundwater, and validated the model for different idealized situations. However, the second group of models is not applied to global-scales but are limited to watershed-, regional-, and continental-scales studies due to high computational costs (Archfield et al., 2015).

The surging interests of applying hyper-resolution LSMs at continental or global scales motivated the development of more comprehensive and efficient representations of subsurface hydrology in LSMs (Archfield et al., 2015). Stemming from the Community Earth System Model (CESM) version 1_3_beta10 (Oleson et al., 2013), the Energy, Exascale, Earth System Model (E3SM) is a state-of-the-art ESM sponsored by the U.S. Department of Energy (Leung et al., 2020). The latest E3SM Land Model version 2.0 (ELMv2.0) solves the 1-D Richard equation in the unsaturated zone based on (Zeng and Decker, 2009) and parameterize the saturated groundwater process with a lumped unconfined aquifer. The goal of this study is to develop and validate a computationally efficient inter-grid cell lateral unsaturated and saturated groundwater flow model within ELMv2.0. Instead of solving the fully 3-D Richards equation, the model solves a modified 1-D θ-based Richards equation including unsaturated and saturated zones, and considers the lateral groundwater flux as a source term. The developed model was first benchmarked against PFLOTRAN (Hammond and Lichtner, 2010) for three idealized hillslope planforms that included a convergent hillslope, divergent hillslope, and titled V-shape hillslope with variable saturated initial conditions. The model was next applied to the Little Washita Watershed (LWW) in the USA to assess its performance with field observations of soil moisture and soil temperature. The impacts of lateral flow on the surface energy fluxes were also evaluated.

2 Methods

2.1 Numerical formulation

2.1.1 Lateral flow in unsaturated zone

In ELMv2.0, the water movement in the unsaturated zone is governed by the 1D θ-based Richards equation given as

$$\frac{\partial \theta}{\partial t} = -\frac{\partial q}{\partial z} - Q \tag{1}$$

where θ [mm^3 mm^{-3}] is the volumetric soil water content, t [s] is time, z [mm] is the height above some datum in the soil column, q [mm s^{-1}] is the water flux, and Q [mm^3 mm^{-3} s^{-1}] is the sink of soil moisture. The flux of water is given by Darcy's law as

$$q = -\kappa \frac{\partial(\psi + z)}{\partial z} \tag{2}$$

https://doi.org/10.5194/egusphere-2023-375
Preprint. Discussion started: 5 April 2023

where k [mm s^{-1}] is the hydraulic conductivity and ψ [mm] is the soil matric potential. The hydraulic conductivity and soil matric potential are modeled as the non-linear function of volumetric soil moisture (Clapp and Hornberger, 1978) as

$$\kappa = \Theta_{ice}\kappa_{sat}\left(\frac{\theta}{\theta_{sat}}\right)^{2B+3} \tag{3a}$$

$$\psi = \psi_{sat}\left(\frac{\theta}{\theta_{sat}}\right)^{-B} \tag{3b}$$

where κ_{sat} [mm s^{-1}] is saturated hydraulic conductivity , ψ_{sat} [mm] is saturated soil matric potential, B is a linear function of percentage clay and organic content (Oleson et al., 2013), and Θ_{ice} is the ice impedance factor (Swenson et al., 2012). ELMv2.0 uses the modified form of Richards equation of Zeng and Decker (2009) that computes Darcy flux as

$$q = -\kappa\frac{\partial(\psi + z - C)}{\partial z} \tag{4}$$

where C is a constant hydraulic potential above the water table, $z_\triangledown$, given as

$$C = \psi_E + z = \psi_{sat}\left[\frac{\theta_E(z)}{\theta_{sat}}\right]^{-B} + z \tag{5}$$

where ψ_E [m] is the equilibrium soil matric potential and θ_E [mm^3 mm^{-3}] is the equilibrium volumetric soil water content. At the water table depth, $z = z_\triangledown$, the soil water content is $\theta_E(z_\triangledown) = \theta_{sat}$, thus $C = \psi_{sat} + z_\triangledown$. Substituting equation (5) in equation (4) leads to

$$q = -\kappa\frac{\partial(\psi - \psi_E)}{\partial z} \tag{6}$$

ELMv2.0 uses finite volume spatial discretization to rewrite the equation 1 as (Oleson et al., 2013):

$$\begin{aligned}\frac{\partial}{\partial t}\int_{\Omega_n}\theta\, dV &= -\int_{\Gamma_n}(\mathbf{q}\cdot\, dA) - \int_{\Omega_n} Q\, dV \\ \left(\frac{\partial\theta_n}{\partial t}\right)V_n &= -\sum_{n'}(\mathbf{q}_{nn'}\cdot\mathbf{A}_{nn'}) - Q_nV_n\end{aligned} \tag{7}$$

where Ω_n represents the n-th non-overlapping control volume with volume V_n, such that $\cup_i^n\Omega_i = \Omega$, Γ_n represents the boundary surface of the n-th control volume. Applying semi-implicit time discretization and based on Taylor series expansion leads to:

$$\begin{aligned}\left(\frac{\Delta\theta_n^{t+1}}{\Delta t}\right)V_n &= -\sum_{n'}(\mathbf{q}_{nn'}^{t+1}\cdot\mathbf{A}_{nn'}) - Q_n^{t+1}V_n \\ \left(\frac{\Delta\theta_n^{t+1}}{\Delta t}\right)V_n &= -\sum_{n'}\left(\mathbf{q}_{nn'}^{t} + \frac{\partial\mathbf{q}_{nn'}^t}{\partial\theta_n}\Delta\theta_n^{t+1} + \frac{\partial\mathbf{q}_{nn'}^t}{\partial\theta_{n'}}\Delta\theta_{n'}^{t+1}\right)\cdot\mathbf{A}_{nn'} - Q_n^{t+1}V_n\end{aligned} \tag{8}$$

where $\Delta\theta_n^{t+1}$ is the change in the volumetric liquid soil moisture over the time interval Δt. Since ELMv2.0 only resolves vertical soil water movement,the control volume n at layer k is connected to the soil layer above and below and has no column

https://doi.org/10.5194/egusphere-2023-375
Preprint. Discussion started: 5 April 2023

connections.The discretized equation 8 leads to a tridiagonal system of equations for each ELM soil column such that at k-th soil layer:

$$a\Delta\theta_{k-1}^{t+1} + b\Delta\theta_{k}^{t+1} + c\Delta\theta_{k+1}^{t+1} = r \tag{9}$$

where:

$$a = -\left(\frac{\partial q_{k-1/2}^{t}}{\partial \theta_{k-1}^{t}}\right) \tag{10}$$

$$b = \left(\frac{\partial q_{k-1/2}^{t}}{\partial \theta_{k}^{t}} - \frac{\partial q_{k+1/2}^{t}}{\partial \theta_{k}^{t}}\right) - \frac{\Delta z_k}{\Delta t} \tag{11}$$

$$c = \left(\frac{\partial q_{k+1/2}^{t}}{\partial \theta_{k+1}^{t}}\right) \tag{12}$$

$$r = -\left(q_{k-1/2}^{t} - q_{k+1/2}^{t} + e_k\right) \tag{13}$$

where $q_{k-1/2}$ mm s^{-1} is the Darcy flux between $k-1$-th and k-th soil layer, Δz_k mm is the soil thickness of the k-th soil layer, and e_k mm s^{-1} is the sink of water.

In this work, we modified the ELMv2.0 tridiagonal system given by equation 9 to include unsaturated lateral flux, q_k^{ulat}, between g-th and g'-th grid cell for the k-th soil layer(Figure 2). The ELM with the newly developed lateral flow model is hereafter abbreviated as ELM$_{lat}$. Specifically, the equation 13 is modified to account for lateral flux, which is explicit time integration and yields

$$r = -\left(q_{k-1/2}^{t} - q_{k+1/2}^{t} + e_k\right) + \sum_{g'}\left(q_k^{ulat,gg'}\right)^{t}\left(\frac{A_k^{gg'}}{V_k^{g}}\right) \tag{14}$$

where $q_k^{ulat,gg'}$ is lateral flux between grid cell g and its neighbor cells g' for the k-th soil layer. The calculation of q^{ulat} is routed based on the connections for each two neighbouring columns. As shown in Figure 1, for a 4-column (marked as x1, x2, x3 and x4) x-z 2-D transect, there are overall 3 connections which are marked as c12, c23, and c34 on the figure. Following Maxwell (2013), we adapt the grid alignment in ELMv2.0 with parallelogram grid cells to better represent the real world terrain. The adaption is illustrated in Figure 1 for a x-z transect with a uniform Δz. In this setup, the lateral Darcy flux in unsaturated zone is modified to follow the grid alignment in Figure 1 (Celia et al., 1990; Maxwell, 2013):

$$q_k^{ulat,gg'} = -\kappa_x\left(\frac{\partial(\psi+z)}{\partial x} cos\theta_x + sin\theta_x\right) \tag{15}$$

where θ_x is the local (cell center) angel of slope at the horizontal (x) direction and θz is the angel between the normal vector of the cell surface and the vertical direction (z) The vertical fluxes including q_z and evapotranspiration (ET)/infiltration are adapted accordingly to align with the terrain following shape as well, which can be expressed as:

$$q_z^{'} = q_z cos\theta_z \tag{16}$$

https://doi.org/10.5194/egusphere-2023-375
Preprint. Discussion started: 5 April 2023

where θ_z is the angle between the normal vector of the cell surface and the vertical direction (z). The lateral Darcy flux at y-direction adopts the same computation method as equation 15. Otherwise, the computation of hydraulic properties and derivatives of the Darcy fluxes relevant to the soil liquid water content follows the same method with Oleson et al. (2013).

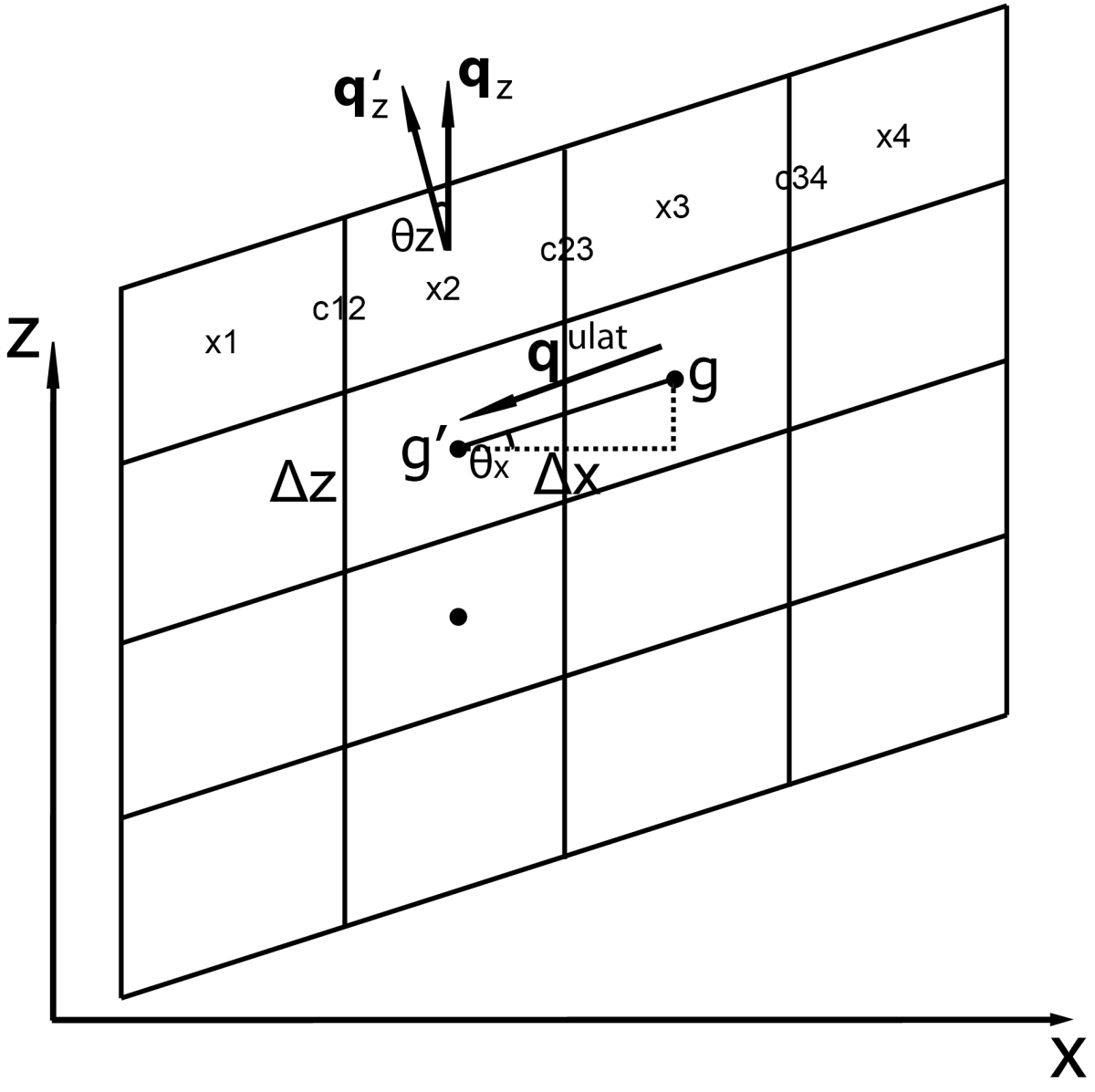

Figure 1. Sketches of the terrain following grid formulations. θx is the local angel of slope at the horizontal (x) direction, and θz is the angle between the normal vector of the cell surface and the vertical direction (z)

https://doi.org/10.5194/egusphere-2023-375
Preprint. Discussion started: 5 April 2023

2.2 Lateral flow in saturated zone

The lateral flow in the saturated zone, q^{slat} $[m^3/s]$, is also modeled using Darcy's law while taking the soil matric potential gradient as the groundwater hydraulic head gradient. In such a manner, the volumetric lateral groundwater flow can be given as:

$$q^{slat} = -wT\frac{\partial z_{\triangledown}}{\partial x} \tag{17}$$

where w [m] is the width of the grid cell, and T $[m^2/s]$ is the transmissivity. The transmissivity is calculated following the method used in Fan et al. (2007). The q^{slat} is computed across inter-grid cell using the same grid cell connections as used for the q^{ulat}. The water table depth for each soil column within a grid cell is thereafter adjusted based on q^{slat}. Specifically, the q^{slat} increases/decreases the soil water content of the soil layer where the groundwater table is currently located. The soil moisture is updated while ensuring the soil moisture remains below/above the maximum/minimum allowable value. If the change in the soil moisture is less than the q^{slat}, the soil moisture of layers above/below is recursively increased/decreased till the total change in soil moisture in all updated soil layers matches q^{slat}. In ELMv2.0, the groundwater table is adjusted by a conceptual recharge flux which depends on whether the water table is within or below the soil column. The approach by explicitly subtracting the hydrostatic equilibrium soil moisture distribution from the Richards equation resolved the numerical deficiencies when the water table is within the soil columns while using θ-based Richards equation (Zeng and Decker, 2009). In ELM$_{lat}$, the water table is assumed within the soil columns, such that the conceptual recharge flux is no longer employed. The groundwater table depth is computed based on the soil water content following the θ-based water table method in CLM5.0 (Figure 2). A no flux boundary condition is applied to the last hydrologically active soil layer. Following ELMv2.0, the saturated zone is depleted by a drainage flux, i.e. the subsurface runoff, that is computed based on the SIMTOP scheme of Niu et al. (2007), with modifications to account for frozen soils (Oleson et al., 2013).

2.3 Model benchmarking against PFLOTRAN for idealized hillslopes

Three idealized hillslopes that included a convergent hillslope (CH), divergent hillslope (DH), and titled V-shape hillslope (VH) with variable saturated initial conditions are used to validate ELM$_{lat}$ by benchmarking against a 3D subsurface flow and transport model, PFLOTRAN (Hammond and Lichtner, 2010).

2.3.1 Idealized hillslope geometries

The CH/DH problems have been widely used to test the newly developed lateral groundwater flow model, e.g. (Troch et al., 2003; An et al., 2010; Hazenberg et al., 2015). Different from ELMv2.0 which uses uniform grid cells, the surface area of CH/DH grid cells change along the slope. The surfaces of CH/DH are curved by the sinusoidal function (Figure 3):

$$z(x,y) = 10\sin\left(\frac{x\pi}{100} - \frac{\pi}{2}\right) + \frac{y}{50} \tag{18}$$

https://doi.org/10.5194/egusphere-2023-375
Preprint. Discussion started: 5 April 2023

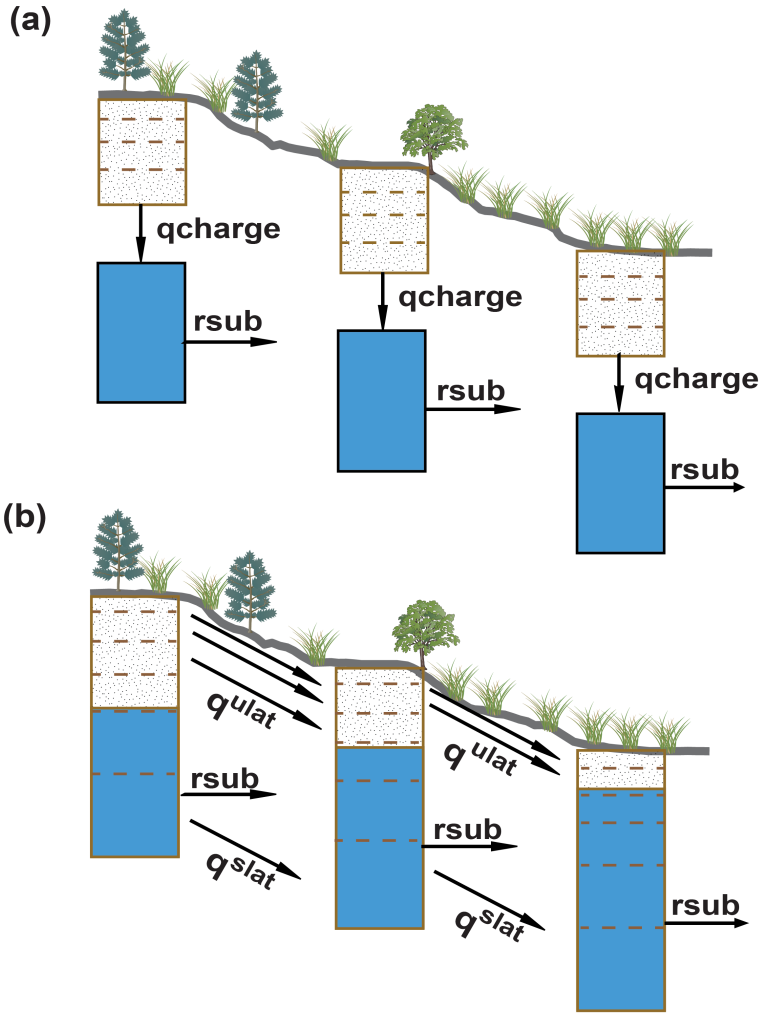

Figure 2. Schematic illustration of the subsurface flow implementation in unsaturated and saturated zone from (a) ELMv2.0 to (b) ELM$_{lat}$; qcharge is the conceptual recharge flux used to update the groundwater table, q^{ulat} is the lateral flux in unsaturated zone, q^{slat} is the lateral flux in saturated zone, rsub is the subsurface runoff

https://doi.org/10.5194/egusphere-2023-375
Preprint. Discussion started: 5 April 2023

where x, y, and z are the coordinates of the cell vertices. For the CH, the total width along the y-direction linearly shrinks from 100 m at hill top to 80 m at hill bottom; whereas for the DH, it linearly expands from 80 m at hill top to 100 m at hill bottom (Figure 3). The total width along the x-direction is 100 m for both CH and DH.

The tilted V-catchment hillslope is another popular benchmark problem for validating groundwater flow in land surface models (Park et al., 2009; Sulis et al., 2011; Maxwell et al., 2014). As shown in Figure 3 (c), the V-shape catchment is formed by the union of two symmetrically inclined planar surfaces (80 m $\times$ 100 m) on the sides connected by a channel in the middle (20 m $\times$ 100 m). The two planar surfaces are inclined with slopes of $\pm$ 0.05 and 0.02 at x and y directions, respectively. The channel is inclined following the slope of 0.02 at the y direction.

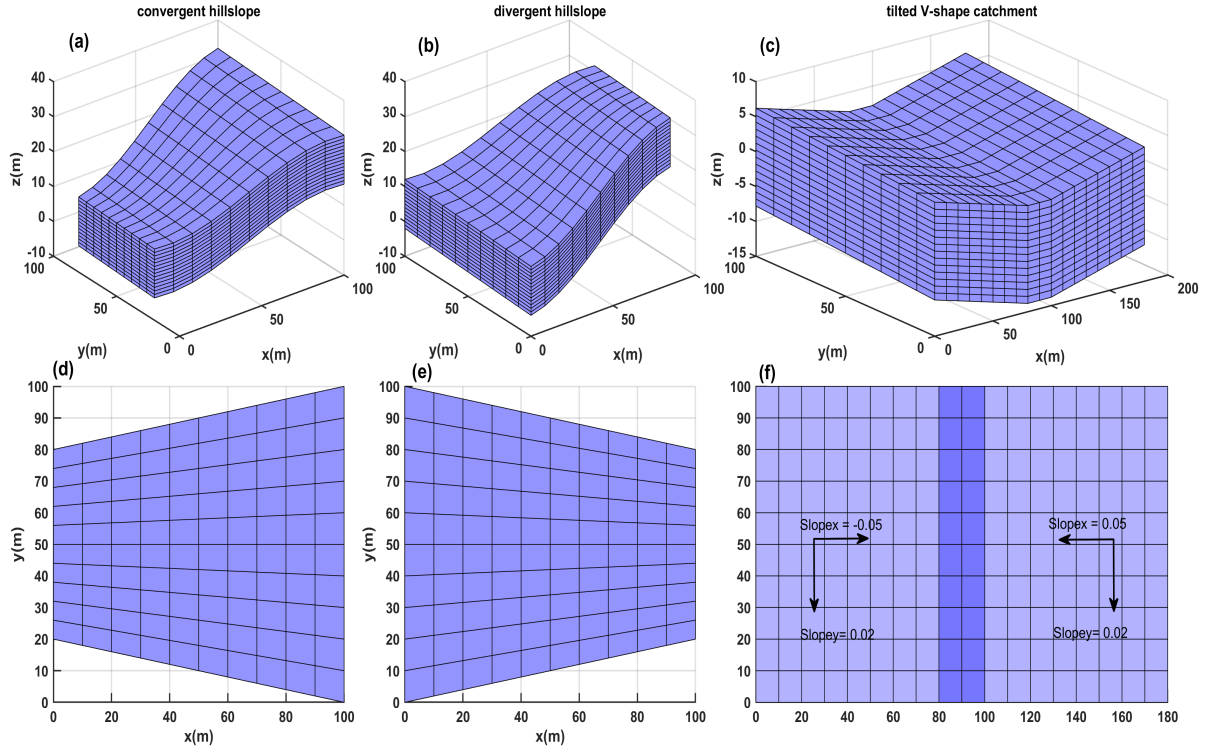

Figure 3. Geometries of the three benchmark test problems. (a), (b), (c) are 3-D views, and (d), (e), (f) are x-y views of the three benchmark test problems, respectively. S_x and S_y are slopes along the x and y directions, respectively.

2.3.2 Model setup

By default, the soil columns of ELMv2.0 are vertically discretized into 15 soil layers of exponentially varying soil thicknesses reaching a depth of 42.1 m. Only the first 10 soil layers are hydrologically active and occupy the top 3.8 m of a soil column.

https://doi.org/10.5194/egusphere-2023-375
Preprint. Discussion started: 5 April 2023

For the model benchmarking, we modified the default model setup by allowing all 15 soil layers to be hydrological active and have a uniform soil thickness of 1 m to be consistent with the setup for PFLOTRAN simulations. The soil columns were horizontally discretized to a 10 × 10 mesh with a grid resolution of 10 m at x direction and changing resolution at y direction for CH and DH. For VH, the soil columns were discretized horizontally with a uniform grid resolution of 10 m at both x and y directions, which produced a mesh of 18 × 10. A homogeneous soil texture was used with a porosity of 0.43. The soil water retention properties in ELMv2.0 were described using the Clapp-Hornberger formula (Clapp and Hornberger, 1978) while in PFLOTRAN they were described using the Brooks Corey's formula (Brooks, 1965). We matched the soil water retention property parameters in PFLOTRAN with ELM. The anisotropic ratio for the hydraulic conductivity was set as 1.0 for the CH and DH cases ($K_x = K_y = K_z$), and was set as 10.0 for the VH case ($K_x = K_y = 10K_z$). The same boundary and initial conditions were applied for the three benchmark problems. A no-flow boundary condition was applied on all sides of the domain. Hydrostatic pressure was used as the initial condition with the groundwater table depth (WTD) set at 7 m deep from the top surface. ELM$_{lat}$ and PFLOTRAN simulations were performed for 80 days for all three benchmark problems and results were compared at the end of the simulation. The performance of soil moisture dynamics was evaluated using the mean absolute error (MAE) between ELM$_{lat}$ and PFLOTRAN, while the performance of groundwater was directly evaluated by the difference between ELM$_{lat}$ and PFLOTRAN simulations.

2.4 Model application

2.4.1 Study region

ELM$_{lat}$ is applied to study the role of lateral subsurface flow on terrestrial processes in the Little Washita Watershed (LWW), which is located in the southwestern Oklahoma, USA (Figure 4). The LWW has a drainage area of ≈611 km^2 and is one of the seven selected experimental watersheds jointly administrated by the U.S. Department of Agriculture (USDA) and U.S. Environmental Protection Agency for a variety of hydrologic research projects. The LWW has a subhumid climate with annual precipitation of approximately 760 mm and annual temperature of approximately 16 °C. The elevation of LWW ranges from approximately 320 m to 460 m., and the slope ranges from 0° to 3° (Figure 4). Grassland is the dominant land cover of LWW, with small portions of land occupied with crops, shrubs, and deciduous trees. The mean annual Leaf Aare Index (LAI) is within the range of 0.5-3 m^2/m^2. Soil textures of LWW are composed of sand, loam, and silty loam (Allen and Naney, 1991). LWW has a relatively higher soil content of sand and organic matter in the northwestern part and southeastern part; several spots in the southern region have higher clay content(Figure 4a-c).

2.4.2 Model configuration and data

The model domain covered a 35 km × 50 km area encompassing the LWW and was laterally discretized at 1 km × 1 km. All 15 soil layers were set as hydrologically active. Results from Fan et al. (2013) show the maximum WTD could reach upto 60 m deep in this region. By default, the 15th soil layer in ELMv2.0 reaches a depth of 48m. Therefore, we modified the soil thickness of the last two soil layers by adding 20 meters each to their default values in ELMv2.0 while keeping the discretization

https://doi.org/10.5194/egusphere-2023-375
Preprint. Discussion started: 5 April 2023

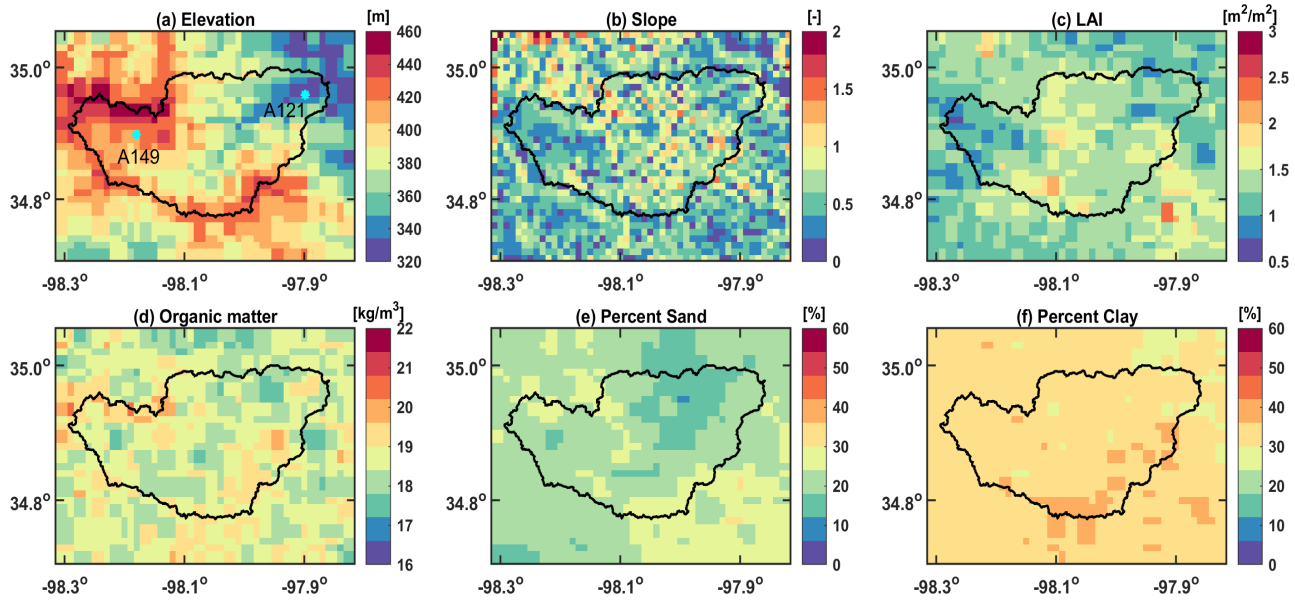

Figure 4. Spatial distributions of (a) elevation, (b) slope, (c) mean monthly leaf area index, (d) organic matter density, and (e–f) percentages of sand and clay, respectively, over the study area at a resolution of 1 km.

of the other 13 soil layers unchanged. The total soil thickness could reach 82 m. The initial WTD was spatially uniformly set at 8 meters deep below the top surface of the domain. The hourly NLDAS data (https://ldas.gsfc.nasa.gov/nldas/v2/forcing) was used as the climate forcing which has a spatial resolution of 1/8th-degree grid. We performed 100-year simulations with ELM$_{lat}$ and ELMv2.0 while cycling the atmospheric forcing data of 2008 to allow sufficient time for the model spin-up. The model results from the last year of the spin-up were used for analysis.

The 1 km surface data used in this study was generated using multiple high-resolution, sub-kilometer data sets including vegetation, soil, and topography related variables (Table 1). The soil, elevation and LAI datasets were first aggregated to 1 km using the area-weighted average method, and the land cover data was aggregated to 1 km using the majority resampling method. Specifically, MODIS 500 m land cover was at year 2005 obtained from the Google Earth Engine (Gorelick et al., 2017). Following Ke et al. (2012), the LC_Type 5 class of MCD12Q1 v6 land cover product (Friedl and Sulla-Menashe, 2019) was used to determine the lake, urban, glacier, and vegetation plant functional types (PFTs). These PFTs were further classified into tropical, temperate, and boreal sub-types based on the rules presented in Bonan et al. (2002) and using meteorological data from WorldClim V1 (Hijmans et al., 2005). The monthly climatology LAI was derived from the 4-day MCD15A3H V6.1 (Myneni et al., 2021) over 2003–2020 using GEE. Then based on the method in Zeng et al. (2002), we calculated the monthly climatology stem area index (SAI) from the LAI data. For the soil data, we used the Soilgrid v2 data with an original resolution of 250 m (Poggio et al., 2021). Soilgrid is generated based on machine learning using multiple data sources of soil profiles and remote sensing data (Hengl et al., 2017). The percent clay, percent sand, and soil organic matter at multiple depths were

https://doi.org/10.5194/egusphere-2023-375
Preprint. Discussion started: 5 April 2023

Table 1. Specifications of high-resolution data sets used in this study.

Type	Parameter	Spatial resolution	Temporal resolution	Data source	Reference
Land cover	Vegetation type	500 m	yearly	MODIS MCD 12Q1 V6	Friedl and Sulla-Menashe (2019)
	leaf area index	500 m	2003–2020, 4-day	MODIS MCD15A3H V6.1	Myneni et al. (2021)
	Stem area index	500 m	2003–2020, 4-day	Calculated	
Soil	Percent sand	250 m	Static	Soilgrid v2	Poggio et al. (2021)
	Percent clay	250 m	Static	Soilgrid v2	Poggio et al. (2021)
	Organic matter	250 m	Static	Soilgrid v2	Poggio et al. (2021)
Topography	Elevation	90 m	Static	SRTM v4	(Jarvis et al., 2008)

processed for ELM. The 90 m digital elevation from the Shuttle Radar Topography Mission (Jarvis et al., 2008) was used to derive topography-related parameters in ELM, including the standard deviation of elevation and slope. These 0.01 deg datasets were processed using GEE based on the original 90 m elevation. We used a continuous global WTD map with a resolution of 30 arc-second (≈1 km) (Fan et al., 2013) to validate the simulated WTD, which is hereafter referred as Fan2013. The impacts of lateral flow on the model performance were assessed by comparing the soil moisture and energy fluxes including soil temperature, Latent and sensible heat flux, with ELMv2.0 simulation. Site-level observations of soil moisture and soil temperature were collected from the ARS Micronetwork (https://ars.mesonet.org/) which is operated and maintained by the USDA.

3 Results and discussion

3.1 Evaluation of simulations for the benchmark problems

ELM$_{lat}$ can accurately reproduce the evolution of vertical soil moisture profile simulated by PFLOTRAN for all three benchmark problems (Figure 5). The model correctly simulates the drying out of uphill soil columns (Figure 5a-b) and the wetting

https://doi.org/10.5194/egusphere-2023-375
Preprint. Discussion started: 5 April 2023

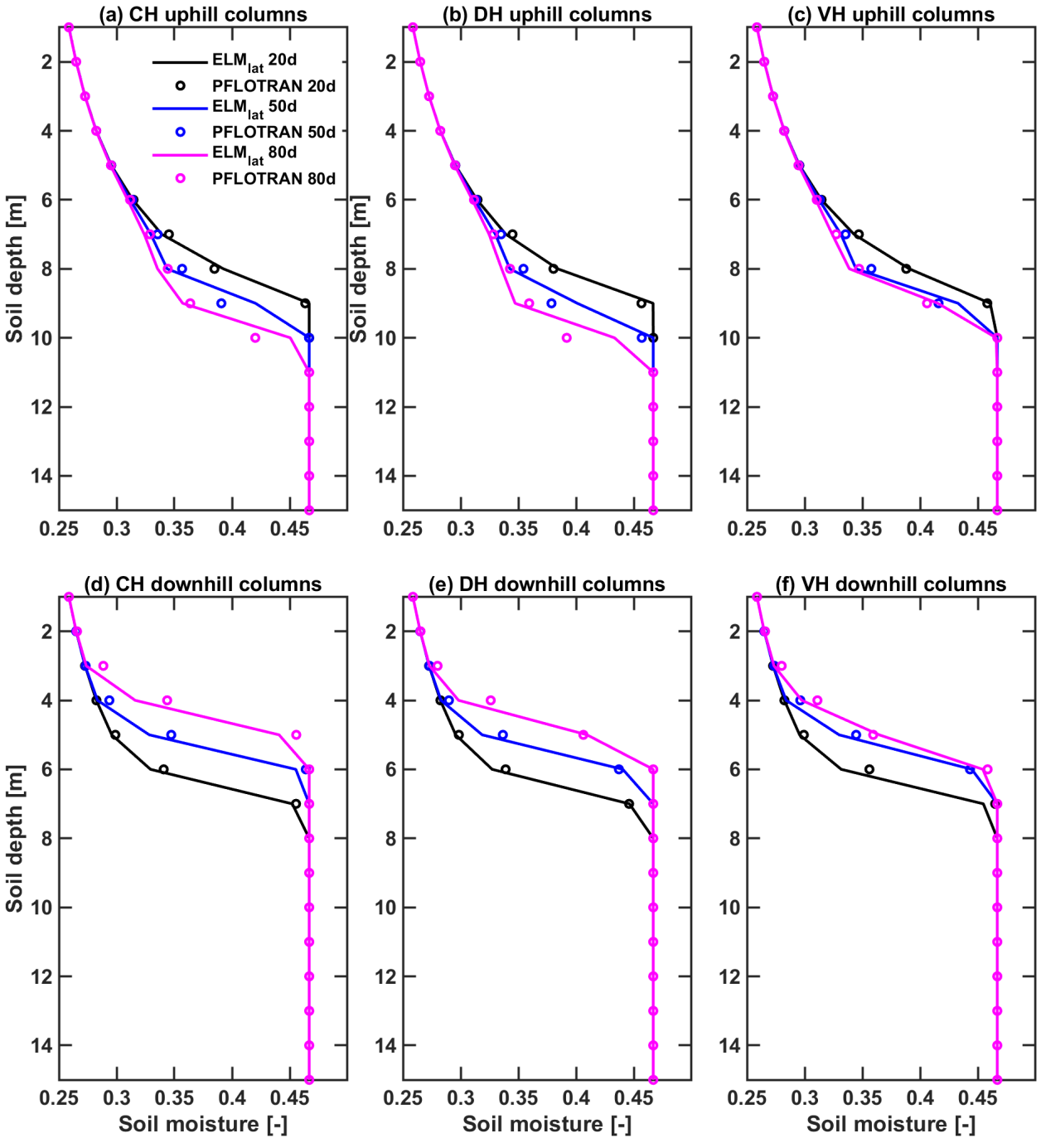

Figure 5. ELM$_{lat}$ simulated mean soil moisture profile for the ten uphill columns of (a) convergent hillslope, (b) divergent hillslope, (c) V-shape hillslope, and ten downhill columns of (d) convergent hillslope, (e) divergent hillslope, (f) V-shape hillslope, at 20th, 50th and 80th simulation day, respectively.

https://doi.org/10.5194/egusphere-2023-375
Preprint. Discussion started: 5 April 2023

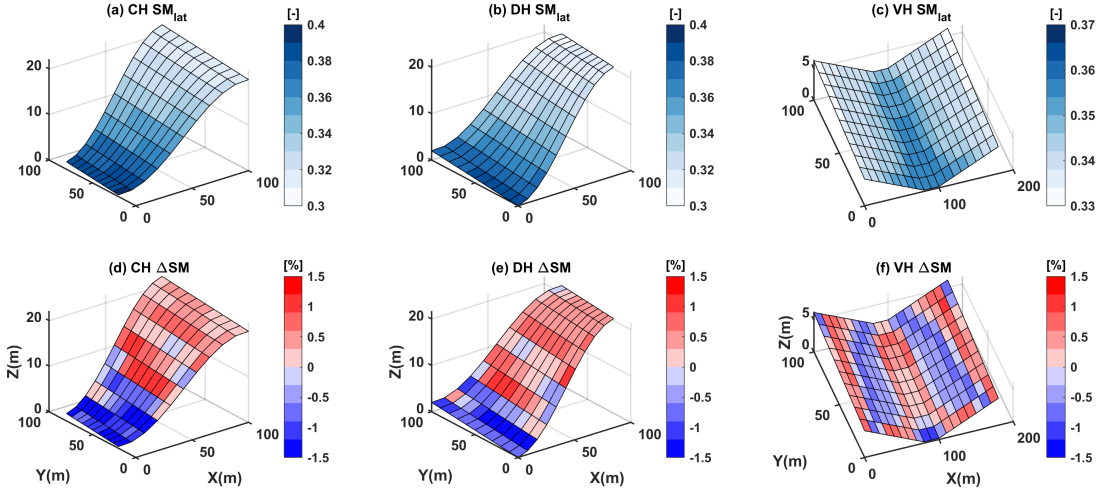

Figure 6. ELM$_{lat}$ simulated average soil moisture for the top 5 layers at $80th$ day for (a) convergent hillslope, (b) divergent hillslope, (c) V-shape hillslope, and the differences with PFLOTRAN for (d) convergent hillslope, (e) divergent hillslope, (f) V-shape hillslope, respectively.

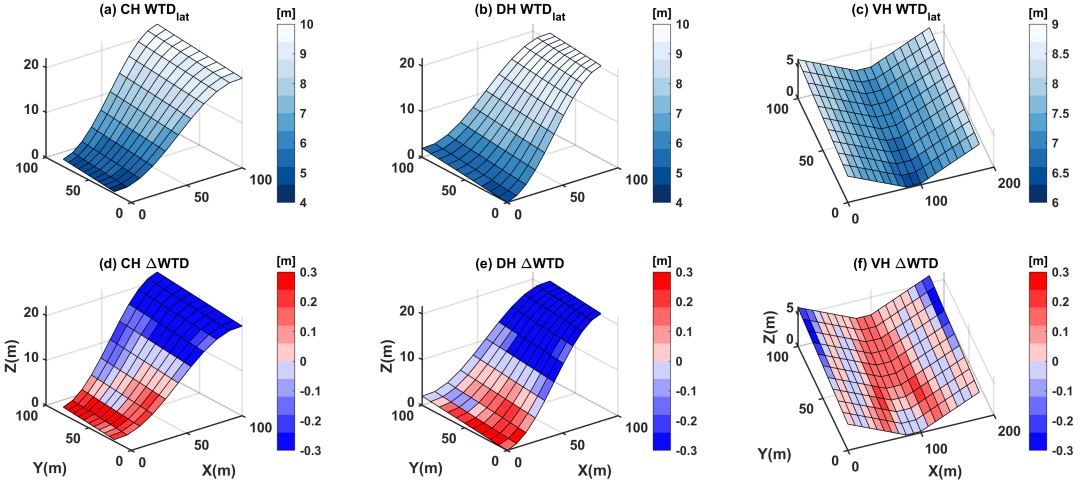

Figure 7. ELM$_{lat}$ simulated water table depth at $80th$ day for (a) convergent hillslope, (b) divergent hillslope, (c) V-shape hillslope, and the differences with PFLOTRAN for (d) convergent hillslope, (e) divergent hillslope, (f) V-shape hillslope, respectively.

https://doi.org/10.5194/egusphere-2023-375
Preprint. Discussion started: 5 April 2023

up of downhill soil columns (Figure 5d-e) for all the three hillslopes. In the VH case, the soil moisture shifted quickly during 20 d – 50 d but slowed down during 50 d – 80 d, whereas the soil moisture changing pace are nearly steady for the CH and DH cases during the two periods. The soil properties used in the three test cases are exactly the same except that the VH case has a higher anisotropic ratio and therefore higher lateral hydraulic conductivity. It is probable that during the period of 50 d - 80 d, the VH case is more approaching hydrostatic condition than the other two cases. These differences were well captured by ELM$_{lat}$ as compared with PFLOTRAN. The largest discrepancies in the simulated soil moisture are in soil layers that are closer to the water table, and these discrepancies could be explained by the differences in the model structure (Figure A1). PFLOTRAN solves the variably saturated subsurface flow equation, which is applicable for both the unsaturated and saturated zones, while ELM$_{lat}$ has two separate flow models for the unsaturated and saturated zone. Thus, the difference between the two models is expected to be the largest near unsaturated-saturated zone transition.

After 80 days evolution, the soil moisture redistributed and transported following the surface topography via the lateral flow (Figure 6a-c). The most downhill columns of CH and DH are approaching saturated. As compared to PFLOTRAN, ELM$_{lat}$ underestimated the soil moisture transport from the upland to the lowland such that the upland cells were wetter and the lowland cells were drier for all three benchmark problems, as shown in Figure 6. However, the difference between the two models was small ($< \pm 2\%$) for the top five layers on the 80-th simulation day, which provides confidence in the ability of ELM$_{lat}$ to simulate lateral unsaturated soil moisture dynamics. During the 80 days simulation period, the MAE in ELM$_{lat}$ simulated soil moisture for all cells in the top 5 soil layers remains within $1\% \pm 4\%$ for all three test problems, as shown in Figure A2.

At the end of the simulation, the simulated groundwater table evolves from the spatially uniform initial depth (i.e., 7 m) to a spatially varying depth that is inversely related to the surface elevation (Figure 7a-c). Similar to the flow in the unsaturated zone, ELM$_{lat}$ underestimates the lateral flow in the saturated zone as compared to PFLOTRAN with a shallower (deeper) simulated groundwater table in upland (lowland) cells (Figure 7d-f). The use of different soil water retention curves (i.e., Clapp and Hornberger (1978) in ELM$_{lat}$ and Brooks (1965) in PFLOTRAN) could account for the differences in simulated WTD. Additionally, it should be noted that the prognostic variable in PFLOTRAN is the soil water pressure and the simulated WTD is diagnosed by linearly interpolating the vertical pressure profile for each soil column. Despite those structural differences, ELM$_{lat}$ simulated WTD is comparable to that of PFLOTRAN with differences within ± 0.3 m throughout the simulation period (Figure A3). Overall, the above evaluation results demonstrate ELM$_{lat}$ could accurately represent vertical and lateral transport of soil moisture and groundwater.

3.2 Evaluation of simulations over LWW

Applying ELM_{lat} in LWW significantly improves the simulation of WTD when compared to the ELMv2.0 results. Simulated WTD by ELM$_{lat}$ showed strong correlations (r = -0.71) with surface topography which is consistent with Fan2013 results, while ELMv2.0-simulated WTD has no spatial variations (Figure 8). The simulated WTD in the higher northwest part of the watershed was not as deep as that reported in Fan2013. One major reason for this could be due to the climate forcing data used in this study may not represent the long term steady state as suggested by Fan2013. Moreover, it has been previously shown that the subsurface drainage parameter (f_d) exerts a strong control on the long-term simulated WTD in 1D ELM

https://doi.org/10.5194/egusphere-2023-375
Preprint. Discussion started: 5 April 2023

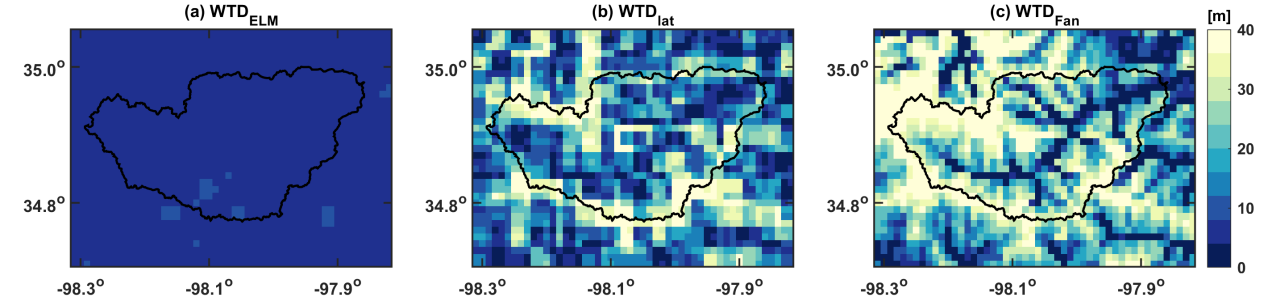

Figure 8. Annual average groundwater table depth (WTD) simulated by (a) ELMv2.0 and (b) ELM$_{lat}$, along with (c) the Fan2013 dataset

simulations (Bisht et al., 2018). However, since the primary goal of this study is to develop the model structure and evaluate the model performance, calibration of f_d to match the Fan2013 results is out of the scope of this work, especially considering the differences of the climate forcings mentioned above. Therefore, no calibration of f_d was done to better match the WTD and the default value of f_d (= 2.5 m^{-1}) was used in this study.

ELM$_{lat}$ simulated generally lower soil temperature (TS) and sensible heat flux (SH) but higher latent heat flux (LH) than ELMv2.0 for most of the grid cells (Figure 9). The spatial annual TS showed a gradually increasing trend from north to south. The LH and SH showed the opposite spatial pattern, where LH is higher the SH is lower. The effects of WTD changes on the energy fluxes were more pronounced at low elevation cells, especially at the stream and its surrounding cells. The delivery of the groundwater through the lateral flow to the valleys supported higher LH while reducing the SH compared with ELMv2.0 which has little spatial WTD variations.

Despite the observations being based on point measurements while simulated results representing 1km resolution, both ELM$_{lat}$ and ELMv2.0 were able to capture the major fluctuations and wetting/drying cycles of soil moisture (SM) comparing with observations at the two stations (Figure 10). Station A121 is located at the lowland area of this catchment with an elevation of 343 m while station A149 is located in the high land area with an elevation of 420 m (Figure 4(a)). At station A121, ELM$_{lat}$ simulated higher soil moisture, with the annual mean 0.013 higher at 5cm and 0.021 higher at 25cm than ELMv2.0 results. At station A149, ELM$_{lat}$ simulated slightly lower soil moisture, with annual mean 0.007 lower at 5cm and 0.009 lower than ELMv2.0 results.

For the soil temperature simulations, we focused on the summer temperature (Figure 11). Relative to ELMv2.0, ELM$_{lat}$ simulated cooler summer temperature at both 5 cm (mean Δ ST = -0.063 $^{\circ}C$) and 30 cm depths (mean Δ ST = -0.061 $^{\circ}C$) at station A121. In contrast, at station A149, ELM$_{lat}$ simulated slightly higher summer temperatures at soil depths of 5 cm (mean Δ ST = 0.018 $^{\circ}C$) and 30 cm (mean Δ ST = 0.019 $^{\circ}C$). The differences in summer temperature between ELM$_{lat}$ and ELMv2.0 were consistent with the SH differences as discussed previously. More water cooled down the summer soil temperature at station A121, whereas less water increased the summer soil temperature at station A149. However, both ELM$_{lat}$ and ELMv2.0 overestimated the temperature during July compared with observations, which may be due to the overestimation of incoming solar radiation or the discrepancies of the soil thermal properties between the model and reality at the sampled locations.

https://doi.org/10.5194/egusphere-2023-375
Preprint. Discussion started: 5 April 2023

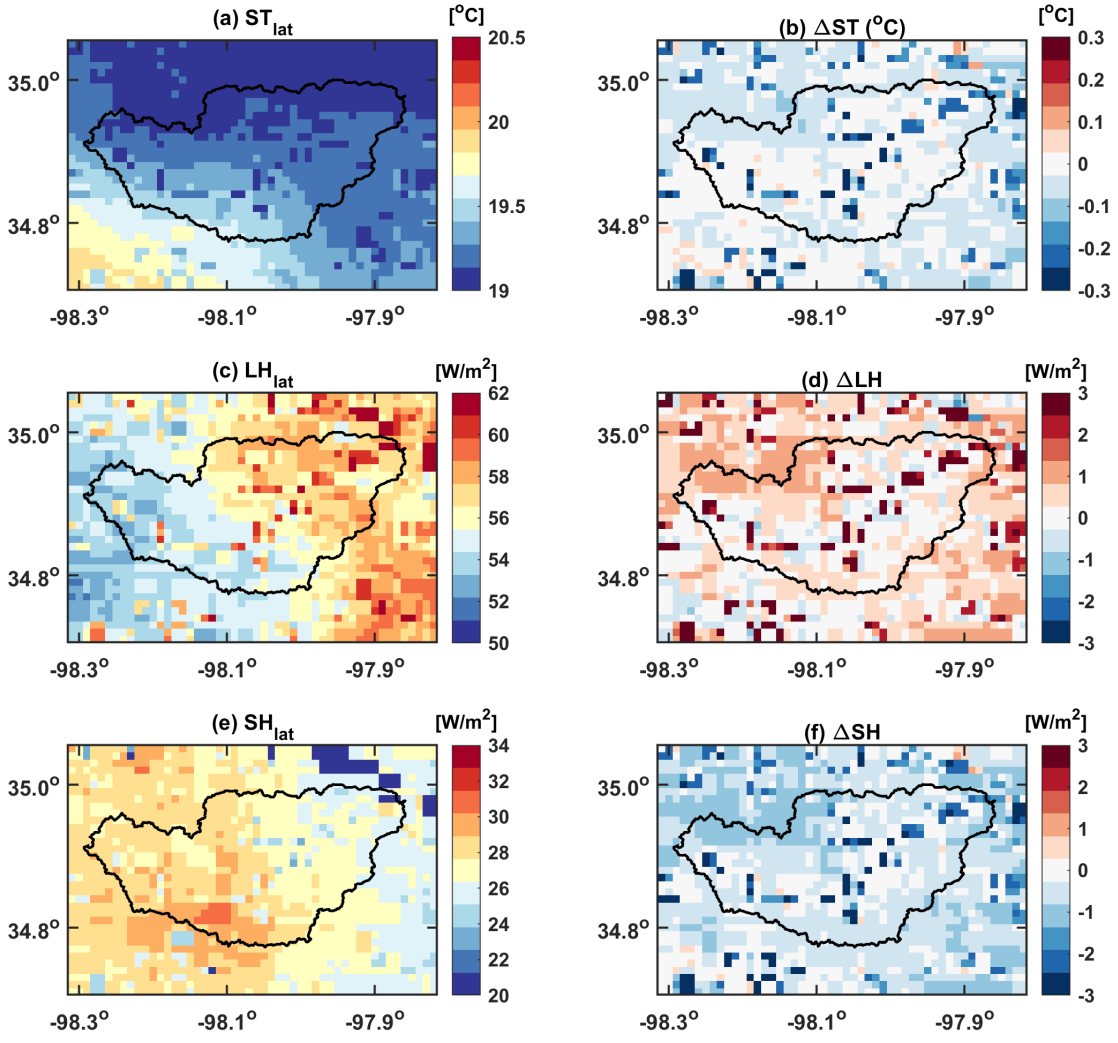

Figure 9. ELM$_{lat}$ simulated annual (a) top layer soil temperature (^oC), (c) latent heat flux (W/m^2) and (e)sensible heat flux (W/m^2); (b), (d), (f) are the differences between ELM$_{lat}$ and ELMv2.0 simulations for the three energy items, respectively

https://doi.org/10.5194/egusphere-2023-375
Preprint. Discussion started: 5 April 2023

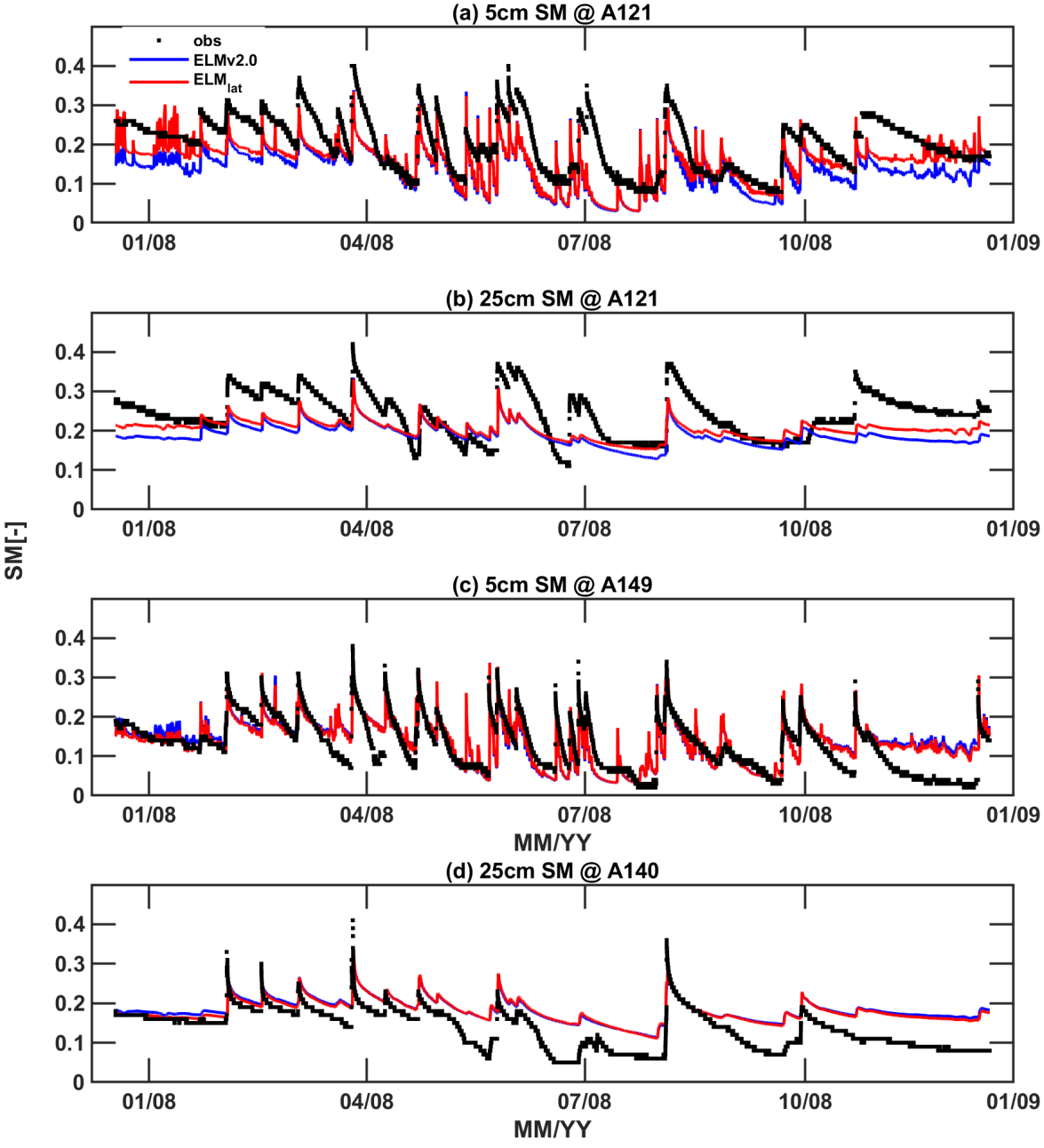

Figure 10. comparisons of simulated hourly soil moisture at depths of (a) 5 cm and (b) 25 cm of a low land station (A121) and at depths of (c) 5 cm and (d) 25 cm of a high land station (A149) between ELM$_{lat}$ and ELMv2.0

https://doi.org/10.5194/egusphere-2023-375
Preprint. Discussion started: 5 April 2023

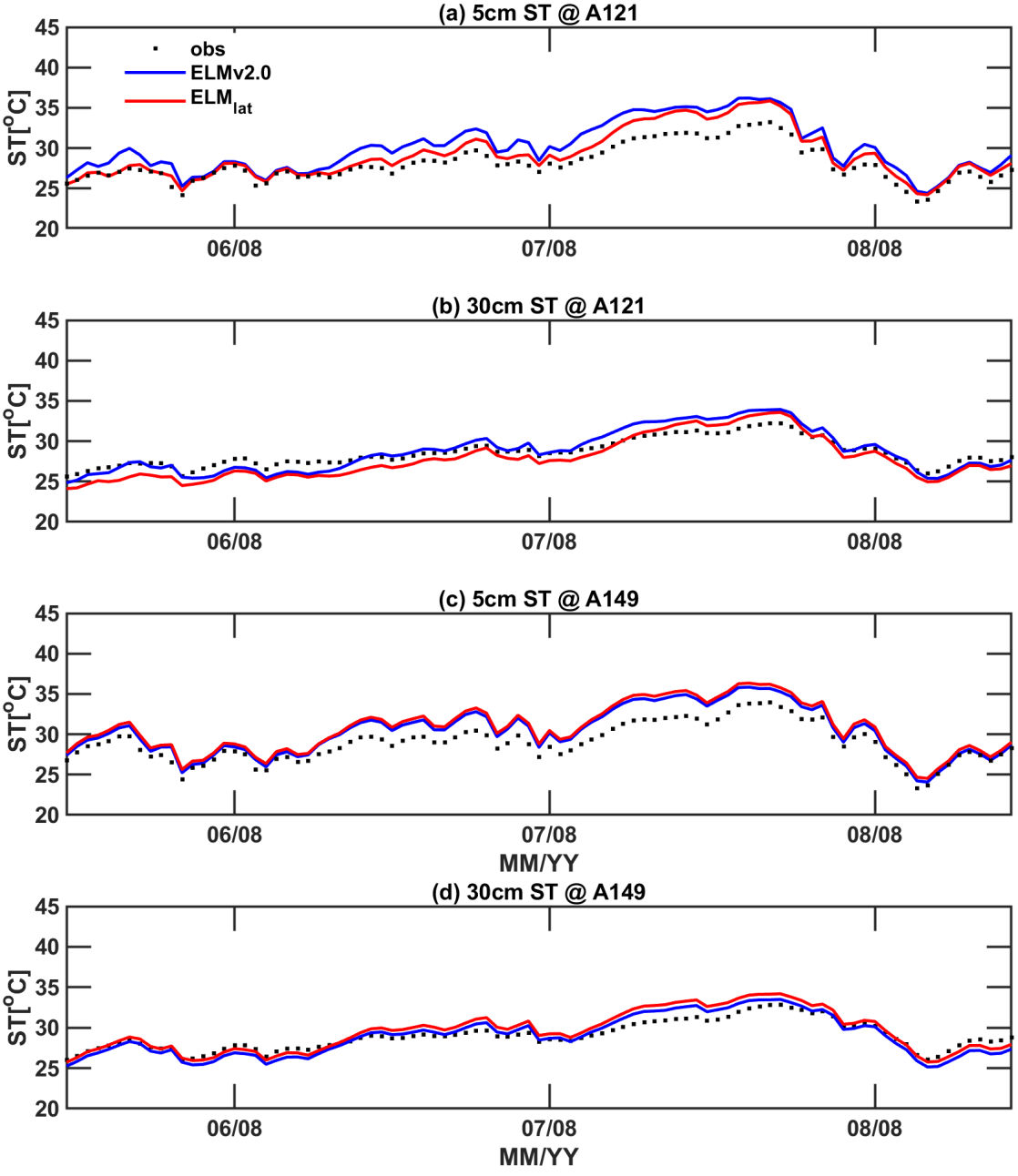

Figure 11. comparisons of simulated hourly summer soil temperature at depths of (a) 5 cm and (b) 25 cm of a low land station (A121) and at depths of (c) 5 cm and (d) 25 cm of a high land station (A149) between ELM$_{lat}$ and ELMv2.0

https://doi.org/10.5194/egusphere-2023-375
Preprint. Discussion started: 5 April 2023

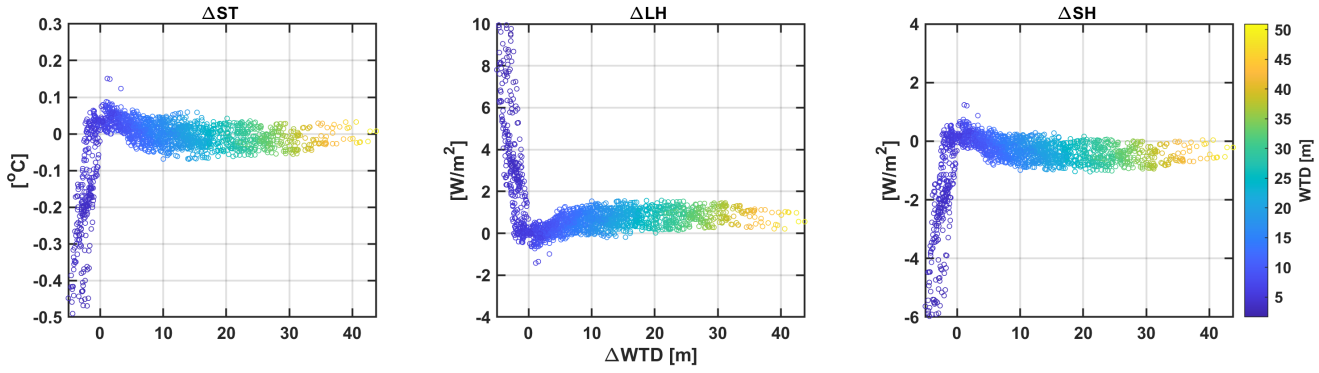

Figure 12. (a), (b), (c) are the difference of annual average surface soil temperature, latent heat flux, and sensible heat flux between ELM-lat and ELMv2.0 vs. simulated groundwater depth differences between ELM$_{lat}$ and ELMv2.0; color bar indicates the groundwater table depths simulated by ELM$_{lat}$

Lateral groundwater flow reshapes the groundwater table map and impacts the surface heat fluxes (Figure 12). The most significant changes between ELM$_{lat}$ and ELMv2.0 in heat fluxes occur when ELM$_{lat}$-simulated WTDs are less than 10 meters, where ELM$_{lat}$ simulated generally shallower WTDs than ELMv2.0. As a result, ELM$_{lat}$ simulated lower surface soil temperature and lower SHs, but higher LHs at shallower WTDs, which are consistent with previous discussions. And the difference of surface soil temperature, LHs and SHs are nearly linearly correlated with the WTD differences when the WTDs are less than 10 meters. At deeper layers, the heat fluxes are not sensitive to changes in WTDs. The maximum differences of simulated surface soil temperature values could reach -0.4−-0.5 $^{\circ}C$, the LHs differences could reach 8−10 W/m^2 and the SHs differences could reach -4−-6 W/m^2, at grids where ELM$_{lat}$ simulated WTDs are less than 5 meters. The depth at which groundwater can influence the vegetation functions are dependent on the roots' penetration depths (Fan, 2015). However, since the land use type is quite simple in this watershed (e.g., mainly grass), it is difficult to differentiate the effects of WTD changes on the vegetation functions for different PFTs.

3.3 Caveats and future work

ELM2.0 parameterizes the subsurface runoff with an exponential relationship of the water table depth (Bisht et al., 2018). Although a spatial uniform value of this parameter was used in this study, the simulated WTD is significantly improved in ELM_{lat} than the default scheme. Calibrating relevant parameters (e.g., f_d) can further improve the representation of WTD in ELM_{lat}. Moreover, a homogeneous anisotropic ratio was assumed in the LWW study given the relatively uniform soil properties. Homogeneous aquifer depth or depth to bedrock (DTB) was also assumed in the LWW study. Brunke et al. (2016) evaluated the effects of using spatially heterogeneous soil thickness and sedimentary deposits (Pelletier et al., 2016) on the simulated hydrological and thermal fluxes in CLM4.5. Incorporating heterogeneous DTB in CLM4.5 has more impacts

https://doi.org/10.5194/egusphere-2023-375
Preprint. Discussion started: 5 April 2023

observed in locations with shallow bedrock than in deep bedrock on the water and energy fluxes, reported by Brunke et al. (2016). Incorporation of variable DTB and evaluation of the heterogeneity of parameters will be performed in the future study.

This study is primarily oriented to validate the new features of the unsaturated and saturated lateral flow in ELM across grids and evaluate the connections between lateral groundwater flow and surface energy fluxes rather than rigidly close the water balance by calibrating all the water balance components against observations. Therefore, water balance and streamflow were not evaluated in this study. A holistic evaluation of the impacts of the lateral groundwater flow on the water and energy balances, as well as the parameter sensitivities, will be tested and evaluated in a much larger domain in the future work. In the present work, we have developed ELM$_{lat}$ that runs serially and the model will be extended in the future to use high performance computing to manage the high computational cost of global simulation.

Additionally, some anthropogenic activities, e.g., groundwater pumping, irrigation, as well as two way river/groundwater interactions are not incorporated into the current model structure. Extensive groundwater pumping reduced discharge to streams, with 10–23% of watersheds reaching critical environmental flow thresholds, revealed from large scale groundwater modeling results (de Graaf et al., 2019). We envision a future road map with more holistic representations of hydrological functions building upon the lateral connections of the grid network, not exclusively the lateral groundwater flow, but more realized groundwater and surface water interactions in ELM.

4 Conclusions

Regarding the emerging highlights of lateral groundwater flow in the hyper-resolution large scale Earth system modeling, we developed and validated an inter-grid cell lateral groundwater flow model for both saturated and unsaturated zone in the E3SM Land Model framework.

By incorporating lateral groundwater flow in the ELMv2.0 and modifying the flux terms based on the non-horizontal terrain, the ELM$_{lat}$ could accurately simulate the soil moisture and WTD dynamics in three idealized hillslope problems validated against PFLOTRAN. The ELM$_{lat}$ underestimates the lateral groundwater flow relative to PFLOTRAN results, which may be attributed to the different formulas used to parameterize the soil water retention properties in the two models. During the simulation period, the MAE between the two models is within $1\% \pm 4\%$, and the simulated WTD differences are within ± 0.3 m.

The developed model was further tested in a realistic watershed, Little Washita Watershed. The simulated WTD by ELM$_{lat}$ showed a strong correlation (r = -0.71) with surface topography where higher land has a deeper groundwater table, which agreed well with the WTD pattern in Fan2013. The effects of lateral groundwater flow on the energy flux partitions were more pronounced at low elevation areas with shallower groundwater tables (i.e., WTD < 10 m). Lateral groundwater movement from highland area to the valleys cooled down the summer surface soil temperature at low land areas; at high land area, less water slightly increased the summer surface soil temperature. More water in the low land area supported higher LH while reducing the SH compared with the ELMv2.0 simulation. In mountain area with very deep WTDs (> 10 m), the movement of lateral fluxes have relatively small effects on the surface energy fluxes relative to the effects at the low land area. These results

https://doi.org/10.5194/egusphere-2023-375
Preprint. Discussion started: 5 April 2023

underscore the importance of including lateral groundwater flow in the LSMs, especially in the critical zone to holistically understand the role of groundwater system on the terrestrial water-energy distribution and its feedback to climate change.

Code and data availability.

Data files and running scripts for model simulations are available at: https://doi.org/10.5281/zenodo.7659300 (Qiu et al., 2023a). ELM$_{lat}$ model are available at:https://doi.org/10.5281/zenodo.7686303 (Qiu et al., 2023b) for the idealized hillslope problems and at:https://doi.org/10.5281/zenodo.7686381 for the LWW application (Qiu et al., 2023c).E3SMv2.0 (including ELMv2.0) is supported by the Linux system.

The details for running E3SMv2.0 (including ELMv2.0) can be found at:https://e3sm.org/model/running-e3sm/e3sm-quick-start/. ELM$_{lat}$ adopts the same compilation and running approaches. PFLOTRAN can be installed and compiled on Linux, Mac, and Windows systems. The detailed instructions for PFLOTRAN installation and running are provided by the user's guidance at:https://www.pflotran.org/documentation/user_guide/user_guide.html

Appendix A

https://doi.org/10.5194/egusphere-2023-375
Preprint. Discussion started: 5 April 2023

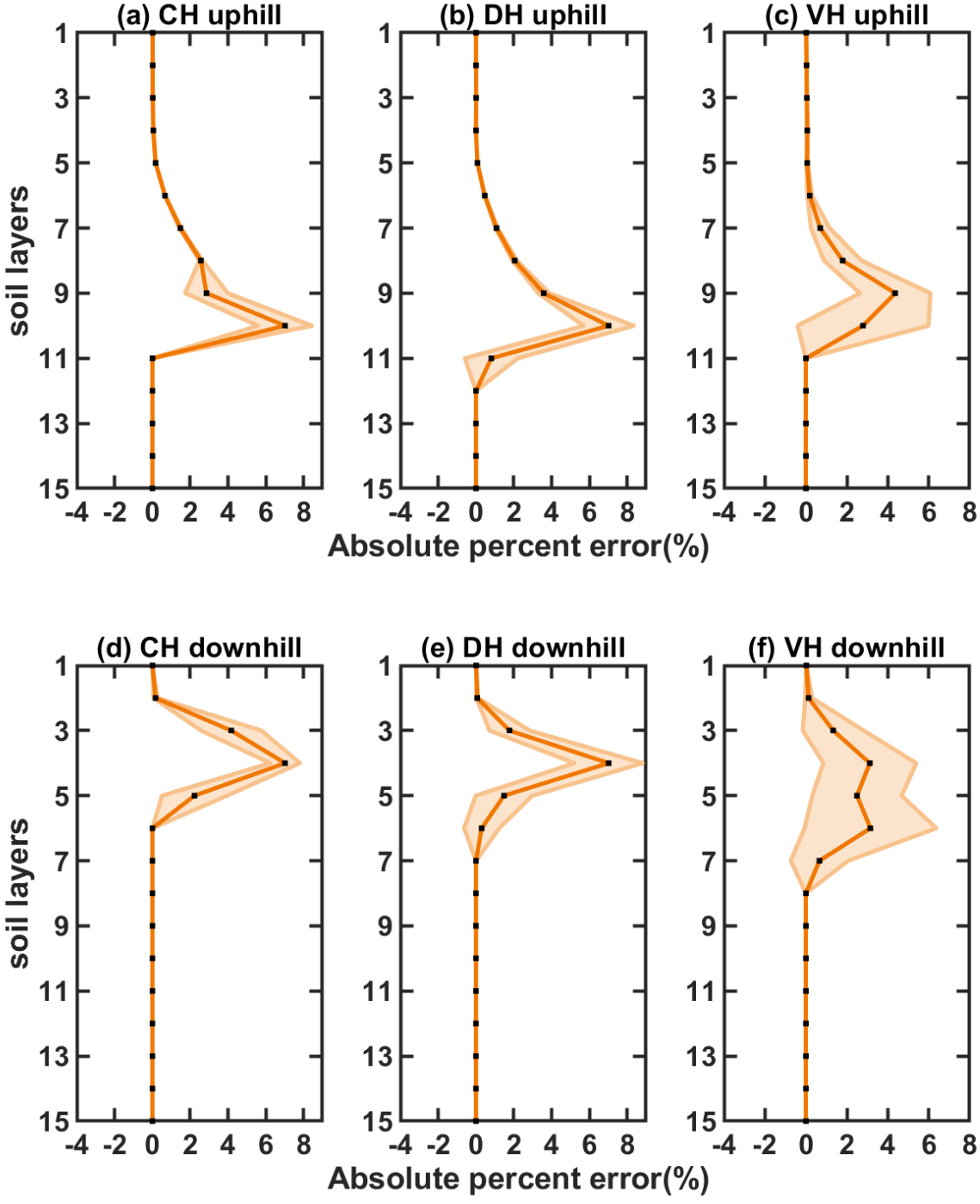

Figure A1. The mean absolute error of simulated soil moisture between ELM$_{lat}$ and PFLOTRAN for the top five soil layers during the simulation period

https://doi.org/10.5194/egusphere-2023-375
Preprint. Discussion started: 5 April 2023

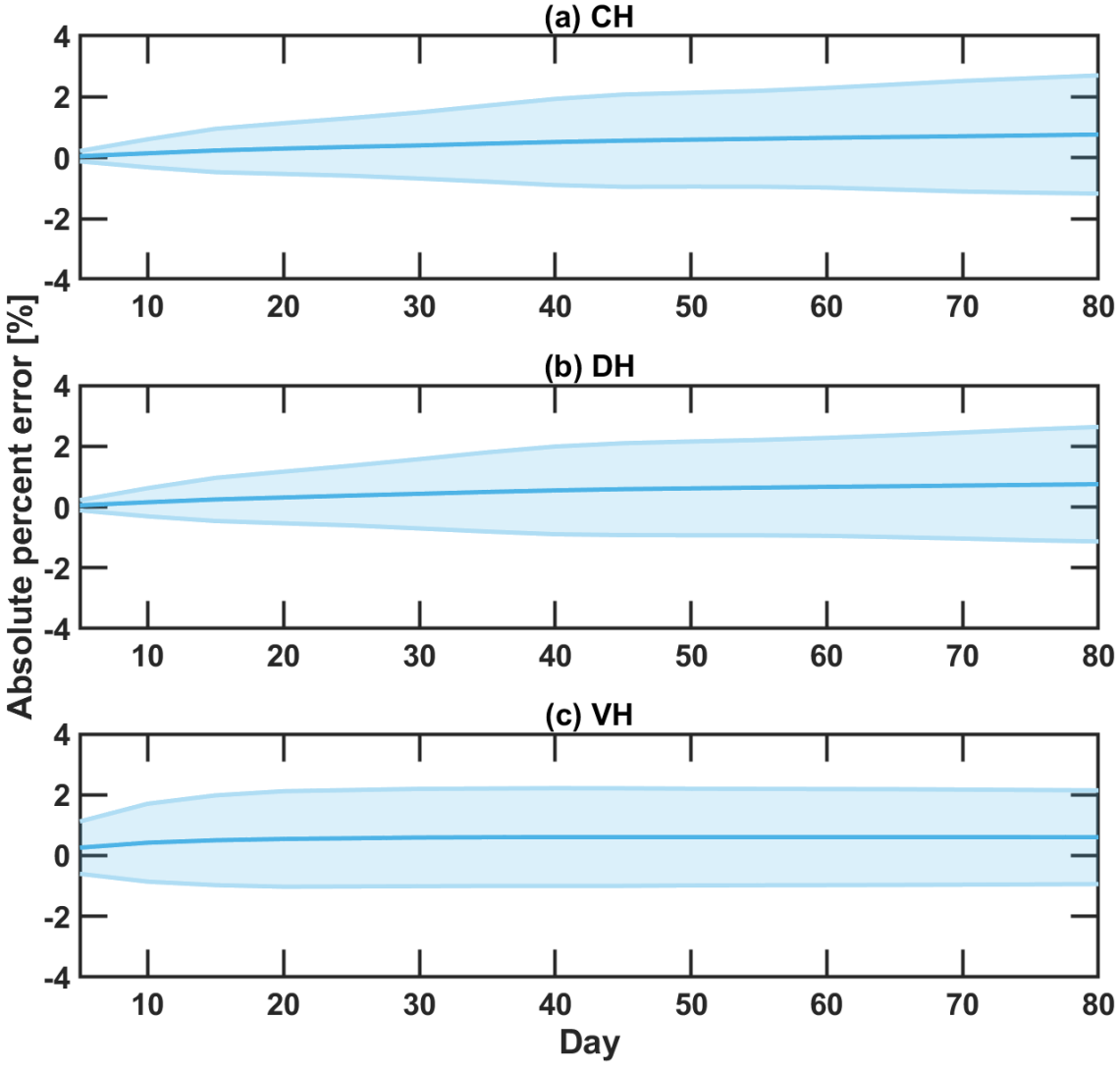

Figure A2. vertical absolute percent errors between ELM_{lat} and PFLOTRAN at the most uphill column for (a) CH, (b) DH, (c) VH and the most downhill column for (d) CH, (e) DH, (f) VH, for each layer at the $80th$ simulation day

https://doi.org/10.5194/egusphere-2023-375
Preprint. Discussion started: 5 April 2023

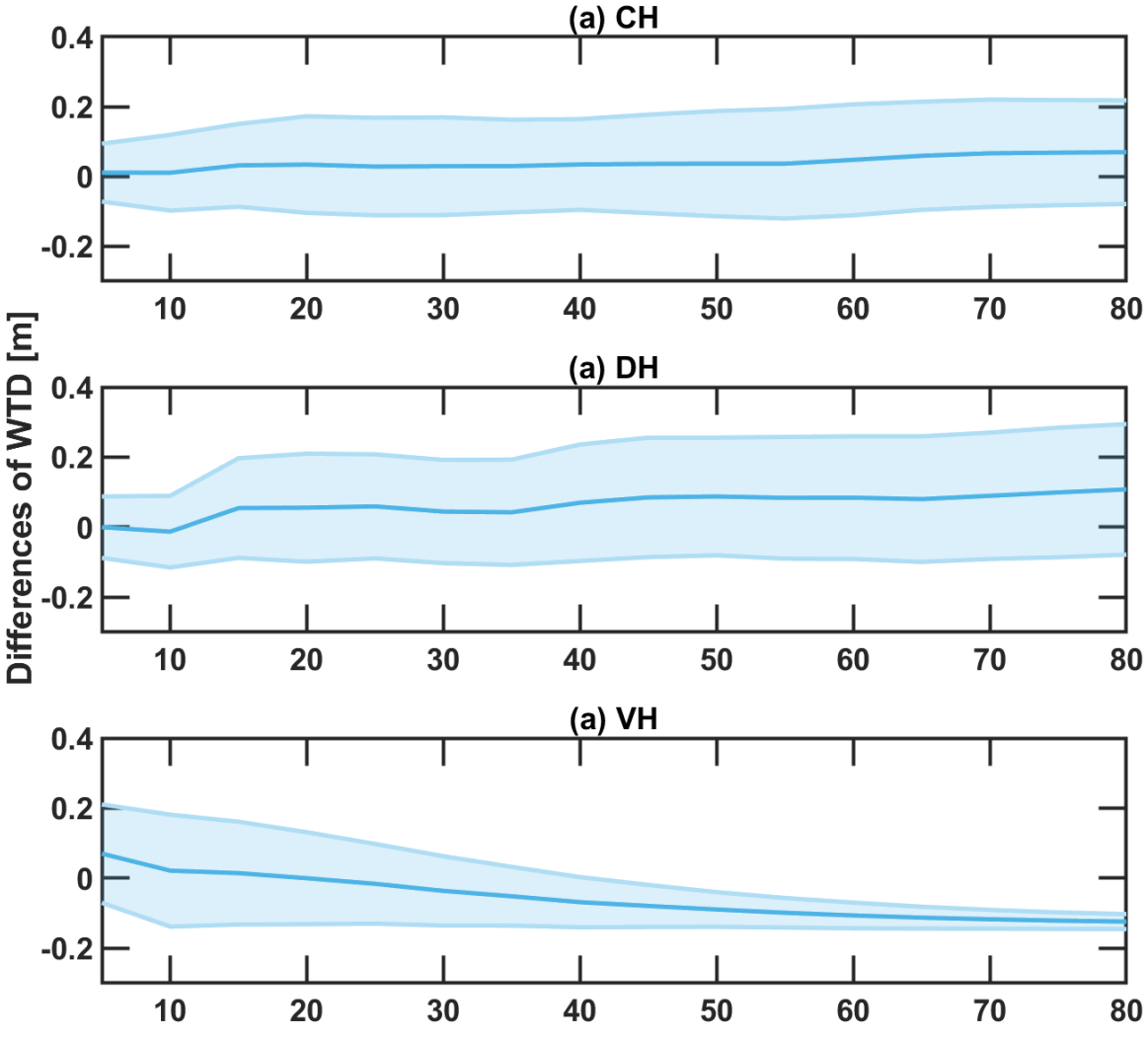

Figure A3. The differences of simulated groundwater table depths between ELM$_{lat}$ and PFLOTRAN during the simulation period

https://doi.org/10.5194/egusphere-2023-375
Preprint. Discussion started: 5 April 2023

Author contributions. HQ designed the study, developed the model, processed the data, and prepared the original manuscript. GB designed the study, discussed the results, and edited the paper LL, DH, and DX processed the data, contributed to subsequent analysis, and helped write and edit the manuscript.

Competing interests. The contact author has declared that none of the authors has any competing interests.

Acknowledgements. The reported research was conducted at Pacific Northwest National Laboratory, which is operated for the U.S. Department of Energy by Battelle Memorial Institute under contract DE-AC05-76RL01830. The simulations for this research were performed on the CompyMcNodeFace, a Department of Energy Office of Biological and Environmental Research's computer system

https://doi.org/10.5194/egusphere-2023-375
Preprint. Discussion started: 5 April 2023

References

Allen, P. B. and Naney, J. W.: Hydrology of the Little Washita River Watershed, Oklahoma:data and analyses, Technical report, Agricultural Research Service, U.S. Dept. of Agriculture, Durant, Ohio, 1991.

An, H., Ichikawa, Y., Tachikawa, Y., and Shiiba, M.: Three-dimensional finite difference saturated-unsaturated flow modeling with nonorthogonal grids using a coordinate transformation method, Water Resources Research, 46, 2010.

Archfield, S. A., Clark, M., Arheimer, B., Hay, L. E., McMillan, H., Kiang, J. E., Seibert, J., Hakala, K., Bock, A., Wagener, T., et al.: Accelerating advances in continental domain hydrologic modeling, Water Resources Research, 51, 10 078–10 091, 2015.

Bierkens, M. F., Bell, V. A., Burek, P., Chaney, N., Condon, L. E., David, C. H., de Roo, A., Döll, P., Drost, N., Famiglietti, J. S., et al.: Hyper-resolution global hydrological modelling: what is next? "Everywhere and locally relevant", Hydrological processes, 29, 310–320, 2015.

Bisht, G., Huang, M., Zhou, T., Chen, X., Dai, H., Hammond, G. E., Riley, W. J., Downs, J. L., Liu, Y., and Zachara, J. M.: Coupling a three-dimensional subsurface flow and transport model with a land surface model to simulate stream–aquifer–land interactions (CP v1. 0), Geoscientific Model Development, 10, 4539–4562, 2017.

Bisht, G., Riley, W. J., Hammond, G. E., and Lorenzetti, D. M.: Development and evaluation of a variably saturated flow model in the global E3SM Land Model (ELM) version 1.0, Geoscientific Model Development, 11, 4085–4102, 2018.

Bonan, G. B., Levis, S., Kergoat, L., and Oleson, K. W.: Landscapes as patches of plant functional types: An integrating concept for climate and ecosystem models, Global Biogeochemical Cycles, 16, 5–1, 2002.

Brooks, R. H.: Hydraulic properties of porous media, Colorado State University, 1965.

Brunke, M. A., Broxton, P., Pelletier, J., Gochis, D., Hazenberg, P., Lawrence, D. M., Leung, L. R., Niu, G.-Y., Troch, P. A., and Zeng, X.: Implementing and evaluating variable soil thickness in the Community Land Model, version 4.5 (CLM4. 5), Journal of climate, 29, 3441–3461, 2016.

Celia, M. A., Bouloutas, E. T., and Zarba, R. L.: A general mass-conservative numerical solution for the unsaturated flow equation, Water resources research, 26, 1483–1496, 1990.

Chaney, N. W., Metcalfe, P., and Wood, E. F.: HydroBlocks: a field-scale resolving land surface model for application over continental extents, Hydrological Processes, 30, 3543–3559, 2016.

Chaney, N. W., Torres-Rojas, L., Vergopolan, N., and Fisher, C. K.: HydroBlocks v0. 2: enabling a field-scale two-way coupling between the land surface and river networks in Earth system models, Geoscientific Model Development, 14, 6813–6832, 2021.

Chui, T. F. M., Low, S. Y., and Liong, S.-Y.: An ecohydrological model for studying groundwater–vegetation interactions in wetlands, Journal of Hydrology, 409, 291–304, 2011.

Clapp, R. B. and Hornberger, G. M.: Empirical equations for some soil hydraulic properties, Water Resources Research, 14, 601–604, https://doi.org/10.1029/WR014i004p00601, 1978.

Clark, M. P., Fan, Y., Lawrence, D. M., Adam, J. C., Bolster, D., Gochis, D. J., Hooper, R. P., Kumar, M., Leung, L. R., Mackay, D. S., et al.: Improving the representation of hydrologic processes in Earth System Models, Water Resources Research, 51, 5929–5956, 2015.

Condon, L. E. and Maxwell, R. M.: Simulating the sensitivity of evapotranspiration and streamflow to large-scale groundwater depletion, Science Advances, 5, eaav4574, 2019.

De Graaf, I., Van Beek, L., Wada, Y., and Bierkens, M.: Dynamic attribution of global water demand to surface water and groundwater resources: Effects of abstractions and return flows on river discharges, Advances in water resources, 64, 21–33, 2014.

https://doi.org/10.5194/egusphere-2023-375
Preprint. Discussion started: 5 April 2023

de Graaf, I. E., van Beek, R. L., Gleeson, T., Moosdorf, N., Schmitz, O., Sutanudjaja, E. H., and Bierkens, M. F.: A global-scale two-layer transient groundwater model: Development and application to groundwater depletion, Advances in water Resources, 102, 53–67, 2017.

de Graaf, I. E., Gleeson, T., Van Beek, L., Sutanudjaja, E. H., and Bierkens, M. F.: Environmental flow limits to global groundwater pumping, Nature, 574, 90–94, 2019.

Döll, P., Hoffmann-Dobrev, H., Portmann, F. T., Siebert, S., Eicker, A., Rodell, M., Strassberg, G., and Scanlon, B.: Impact of water withdrawals from groundwater and surface water on continental water storage variations, Journal of Geodynamics, 59, 143–156, 2012.

Eyring, V., Bony, S., Meehl, G. A., Senior, C. A., Stevens, B., Stouffer, R. J., and Taylor, K. E.: Overview of the Coupled Model Intercomparison Project Phase 6 (CMIP6) experimental design and organization, Geoscientific Model Development, 9, 1937–1958, 2016.

Fan, Y.: Groundwater in the E arth's critical zone: Relevance to large-scale patterns and processes, Water Resources Research, 51, 3052–3069, 2015.

Fan, Y., Miguez-Macho, G., Weaver, C. P., Walko, R., and Robock, A.: Incorporating water table dynamics in climate modeling: 1. Water table observations and equilibrium water table simulations, Journal of Geophysical Research: Atmospheres, 112, 2007.

Fan, Y., Li, H., and Miguez-Macho, G.: Global patterns of groundwater table depth, Science, 339, 940–943, 2013.

Fan, Y., Clark, M., Lawrence, D. M., Swenson, S., Band, L., Brantley, S. L., Brooks, P. D., Dietrich, W. E., Flores, A., Grant, G., et al.: Hillslope hydrology in global change research and earth system modeling, Water Resources Research, 55, 1737–1772, 2019.

Fang, K., Shen, C., Fisher, J. B., and Niu, J.: Improving Budyko curve-based estimates of long-term water partitioning using hydrologic signatures from GRACE, Water Resources Research, 52, 5537–5554, 2016.

Fang, Y., Leung, L. R., Koven, C. D., Bisht, G., Detto, M., Cheng, Y., McDowell, N., Muller-Landau, H., Wright, S. J., and Chambers, J. Q.: Modeling the topographic influence on aboveground biomass using a coupled model of hillslope hydrology and ecosystem dynamics, Geoscientific Model Development, 15, 7879–7901, 2022.

Felfelani, F., Lawrence, D. M., and Pokhrel, Y.: Representing intercell lateral groundwater flow and aquifer pumping in the community land model, Water Resources Research, 57, e2020WR027 531, 2021.

Friedl, M. A. and Sulla-Menashe, D.: MMCD12Q1 MODIS/Terra+Aqua Land Cover Type Yearly L3 Global 500m SIN Grid V006 [Data set], Tech. rep., NASA EOSDIS Land Processes DAAC, https://doi.org/10.5067/MODIS/MCD12Q1.006 (accessed Nov 21 , 2022)., 2019.

Gleeson, T., Wada, Y., Bierkens, M. F., and Van Beek, L. P.: Water balance of global aquifers revealed by groundwater footprint, Nature, 488, 197–200, 2012.

Gorelick, N., Hancher, M., Dixon, M., Ilyushchenko, S., Thau, D., and Moore, R.: Google Earth Engine: Planetary-scale geospatial analysis for everyone, Remote sensing of Environment, 202, 18–27, 2017.

Hammond, G. E. and Lichtner, P. C.: Field-scale model for the natural attenuation of uranium at the Hanford 300 Area using high-performance computing, Water Resources Research, 46, 2010.

Hazenberg, P., Fang, Y., Broxton, P., Gochis, D., Niu, G.-Y., Pelletier, J., Troch, P., and Zeng, X.: A hybrid-3D hillslope hydrological model for use in E arth system models, Water Resources Research, 51, 8218–8239, 2015.

Hengl, T., Mendes de Jesus, J., Heuvelink, G. B., Ruiperez Gonzalez, M., Kilibarda, M., Blagotić, A., Shangguan, W., Wright, M. N., Geng, X., Bauer-Marschallinger, B., et al.: SoilGrids250m: Global gridded soil information based on machine learning, PLoS one, 12, e0169 748, 2017.

Hijmans, R. J., Cameron, S. E., Parra, J. L., Jones, P. G., and Jarvis, A.: Very high resolution interpolated climate surfaces for global land areas, International Journal of Climatology: A Journal of the Royal Meteorological Society, 25, 1965–1978, 2005.

https://doi.org/10.5194/egusphere-2023-375
Preprint. Discussion started: 5 April 2023

Jarvis, A., Reuter, H. I., Nelson, A., Guevara, E., et al.: Hole-filled SRTM for the globe Version 4, available from the CGIAR-CSI SRTM 90m Database (http://srtm. csi. cgiar. org), 15, 5, 2008.

Ke, Y., Leung, L., Huang, M., Coleman, A. M., Li, H., and Wigmosta, M. S.: Development of high resolution land surface parameters for the Community Land Model, Geoscientific Model Development, 5, 1341–1362, 2012.

Kløve, B., Ala-Aho, P., Bertrand, G., Gurdak, J. J., Kupfersberger, H., Kværner, J., Muotka, T., Mykrä, H., Preda, E., Rossi, P., et al.: Climate change impacts on groundwater and dependent ecosystems, Journal of Hydrology, 518, 250–266, 2014.

Kollet, S. J. and Maxwell, R. M.: Integrated surface–groundwater flow modeling: A free-surface overland flow boundary condition in a parallel groundwater flow model, Advances in Water Resources, 29, 945–958, 2006.

Kollet, S. J. and Maxwell, R. M.: Capturing the influence of groundwater dynamics on land surface processes using an integrated, distributed watershed model, Water Resources Research, 44, 2008.

Krakauer, N. Y., Li, H., and Fan, Y.: Groundwater flow across spatial scales: importance for climate modeling, Environmental Research Letters, 9, 034 003, 2014.

Leung, L. R., Bader, D. C., Taylor, M. A., and McCoy, R. B.: An introduction to the E3SM special collection: Goals, science drivers, development, and analysis, Journal of Advances in Modeling Earth Systems, 12, e2019MS001 821, 2020.

Maxwell, R. M.: A terrain-following grid transform and preconditioner for parallel, large-scale, integrated hydrologic modeling, Advances in Water Resources, 53, 109–117, 2013.

Maxwell, R. M., Chow, F. K., and Kollet, S. J.: The groundwater–land-surface–atmosphere connection: Soil moisture effects on the atmospheric boundary layer in fully-coupled simulations, Advances in Water Resources, 30, 2447–2466, 2007.

Maxwell, R. M., Putti, M., Meyerhoff, S., Delfs, J.-O., Ferguson, I. M., Ivanov, V., Kim, J., Kolditz, O., Kollet, S. J., Kumar, M., et al.: Surface-subsurface model intercomparison: A first set of benchmark results to diagnose integrated hydrology and feedbacks, Water resources research, 50, 1531–1549, 2014.

Miguez-Macho, G. and Fan, Y.: The role of groundwater in the Amazon water cycle: 1. Influence on seasonal streamflow, flooding and wetlands, Journal of Geophysical Research: Atmospheres, 117, 2012.

Miguez-Macho, G., Fan, Y., Weaver, C. P., Walko, R., and Robock, A.: Incorporating water table dynamics in climate modeling: 2. Formulation, validation, and soil moisture simulation, Journal of Geophysical Research: Atmospheres, 112, 2007.

Miura, Y. and Yoshimura, K.: Development and verification of a three-dimensional variably saturated flow model for assessment of future global water resources, Journal of Advances in Modeling Earth Systems, 12, e2020MS002 093, 2020.

Myneni, R., Yuri, K., and Park, T.: MODIS/Terra+Aqua Leaf Area Index/FPAR 4-Day L4 Global 500m SIN Grid V061 [Data set], Tech. rep., NASA EOSDIS Land Processes DAAC, https://doi.org/10.5067/MODIS/MCD15A3H.061 (accessed Nov 21 , 2022)., 2021.

Niu, G.-Y., Yang, Z.-L., Dickinson, R. E., Gulden, L. E., and Su, H.: Development of a simple groundwater model for use in climate models and evaluation with Gravity Recovery and Climate Experiment data, Journal of Geophysical Research: Atmospheres, 112, n/a–n/a, https://doi.org/10.1029/2006JD007522, 2007.

Oleson, K. W., Lawrence, D., Bonan, G. B., Drewniak, B., Huang, M., Koven, C. D., Levis, S., Li, F., Riley, W. J., Subin, Z. M., Swenson, S. C., Thornton, P. E., Bozbiyik, A., Fisher, R., Kluzek, E., Lamarque, J.-F., Lawrence, P., Leung, L., Lipscomb, W., Muszala, S., Ricciuto, D., Sacks, W., Sun, Y., Tang, J., and Yang, Z.-L.: Technical Description of version 4.5 of the Community Land Model (CLM), Ncar Technical Note NCAR TN-503+STR, National Center for Atmospheric Research, Boulder, CO, https://doi.org/10.5065/D6RR1W7M, 2013.

https://doi.org/10.5194/egusphere-2023-375
Preprint. Discussion started: 5 April 2023

Paniconi, C., Troch, P. A., van Loon, E. E., and Hilberts, A. G.: Hillslope-storage Boussinesq model for subsurface flow and variable source areas along complex hillslopes: 2. Intercomparison with a three-dimensional Richards equation model, Water Resources Research, 39, 2003.

Park, Y.-J., Sudicky, E. A., Panday, S., and Matanga, G.: Implicit Subtime Stepping for Solving Nonlinear Flow Equations in an Integrated Surface–Subsurface SystemAll rights reserved. No part of this periodical may be reproduced or transmitted in any form or by any means, electronic or mechanical, including photocopying, recording, or any information storage and retrieval system, without permission in writing from the publisher., Vadose Zone Journal, 8, 825–836, 2009.

Pelletier, J. D., Broxton, P. D., Hazenberg, P., Zeng, X., Troch, P. A., Niu, G.-Y., Williams, Z., Brunke, M. A., and Gochis, D.: A gridded global data set of soil, intact regolith, and sedimentary deposit thicknesses for regional and global land surface modeling, Journal of Advances in Modeling Earth Systems, 8, 41–65, 2016.

Poggio, L., De Sousa, L. M., Batjes, N. H., Heuvelink, G., Kempen, B., Ribeiro, E., and Rossiter, D.: SoilGrids 2.0: producing soil information for the globe with quantified spatial uncertainty, Soil, 7, 217–240, 2021.

Pokhrel, Y. N., Koirala, S., Yeh, P. J.-F., Hanasaki, N., Longuevergne, L., Kanae, S., and Oki, T.: Incorporation of groundwater pumping in a global L and S urface M odel with the representation of human impacts, Water Resources Research, 51, 78–96, 2015.

Qiu, H., Blaen, P., Comer-Warner, S., Hannah, D. M., Krause, S., and Phanikumar, M. S.: Evaluating a coupled phenology-surface energy balance model to understand stream-subsurface temperature dynamics in a mixed-use farmland catchment, Water Resources Research, 55, 1675–1697, 2019.

Qiu, H., G.Bisht, L.Li, D.Hao, and D.Xu: ELM Lateral Groundwater Flow model documents, Documents, https://doi.org/https://doi.org/10.5281/zenodo.7659300, 2023a.

Qiu, H., G.Bisht, L.Li, D.Hao, and D.Xu: ELM-lateral-gw-flow for idealized hillslopes, Software, https://doi.org/https://doi.org/10.5281/zenodo.7659303, 2023b.

Qiu, H., G.Bisht, L.Li, D.Hao, and D.Xu: ELM lateral groundwater flow codes, Software, https://doi.org/https://doi.org/10.5281/zenodo.7686381, 2023c.

Richards, L. A.: Capillary conduction of liquids through porous mediums, Physics, 1, 318–333, 1931.

Shen, C. and Phanikumar, M. S.: A process-based, distributed hydrologic model based on a large-scale method for surface–subsurface coupling, Advances in Water Resources, 33, 1524–1541, 2010.

Shen, C., Niu, J., and Phanikumar, M. S.: Evaluating controls on coupled hydrologic and vegetation dynamics in a humid continental climate watershed using a subsurface-land surface processes model, Water Resources Research, 49, 2552–2572, 2013.

Subin, Z., Milly, P. C., Sulman, B., Malyshev, S., and Shevliakova, E.: Resolving terrestrial ecosystem processes along a subgrid topographic gradient for an earth-system model, Hydrology and Earth System Sciences Discussions, 11, 8443–8492, 2014.

Sulis, M., Paniconi, C., Rivard, C., Harvey, R., and Chaumont, D.: Assessment of climate change impacts at the catchment scale with a detailed hydrological model of surface-subsurface interactions and comparison with a land surface model, Water Resources Research, 47, 2011.

Swenson, S. C., Lawrence, D. M., and Lee, H.: Improved simulation of the terrestrial hydrological cycle in permafrost regions by the Community Land Model, Journal of Advances in Modeling Earth Systems, 4, n/a–n/a, https://doi.org/10.1029/2012MS000165, m08002, 2012.

Swenson, S. C., Clark, M., Fan, Y., Lawrence, D. M., and Perket, J.: Representing intrahillslope lateral subsurface flow in the community land model, Journal of Advances in Modeling Earth Systems, 11, 4044–4065, 2019.

https://doi.org/10.5194/egusphere-2023-375
Preprint. Discussion started: 5 April 2023

Troch, P. A., Paniconi, C., van Loon, E., and E: Hillslope-storage Boussinesq model for subsurface flow and variable source areas along complex hillslopes: 1. Formulation and characteristic response, Water Resources Research, 39, 2003.

Vrettas, M. D. and Fung, I. Y.: Sensitivity of transpiration to subsurface properties: Exploration with a 1-D model, Journal of Advances in Modeling Earth Systems, 9, 1030–1045, 2017.

Wada, Y., Van Beek, L. P., Van Kempen, C. M., Reckman, J. W., Vasak, S., and Bierkens, M. F.: Global depletion of groundwater resources, Geophysical research letters, 37, 2010.

Wada, Y., Van Beek, L., and Bierkens, M. F.: Modelling global water stress of the recent past: on the relative importance of trends in water demand and climate variability, Hydrology and Earth System Sciences, 15, 3785–3808, 2011.

Wada, Y., van Beek, L. P., and Bierkens, M. F.: Nonsustainable groundwater sustaining irrigation: A global assessment, Water Resources Research, 48, 2012.

Wang, D.: Evaluating interannual water storage changes at watersheds in Illinois based on long-term soil moisture and groundwater level data, Water Resources Research, 48, 2012.

Wood, E. F., Roundy, J. K., Troy, T. J., Van Beek, L., Bierkens, M. F., Blyth, E., de Roo, A., Döll, P., Ek, M., Famiglietti, J., et al.: Hyperresolution global land surface modeling: Meeting a grand challenge for monitoring Earth's terrestrial water, Water Resources Research, 47, 2011.

Zeng, X. and Decker, M.: Improving the Numerical Solution of Soil MoistureâBased Richards Equation for Land Models with a Deep or Shallow Water Table, Journal of Hydrometeorology, 10, 308–319, https://doi.org/10.1175/2008JHM1011.1, 2009.

Zeng, X., Shaikh, M., Dai, Y., Dickinson, R. E., and Myneni, R.: Coupling of the common land model to the NCAR community climate model, Journal of Climate, 15, 1832–1854, 2002.

Zeng, Y., Xie, Z., Liu, S., Xie, J., Jia, B., Qin, P., and Gao, J.: Global land surface modeling including lateral groundwater flow, Journal of Advances in Modeling Earth Systems, 10, 1882–1900, 2018.

Zhang, J., Feng, Z., Niu, J., Melack, J. M., Zhang, J., Qiu, H., Hu, B. X., and Riley, W. J.: Spatiotemporal variations of evapotranspiration in Amazonia using the wavelet phase difference analysis, Journal of Geophysical Research: Atmospheres, 127, e2021JD034 959, 2022.